

Editor Decision: Publish subject to technical corrections (28 Oct 2015) by William Lahoz

Comments to the Author:

The authors should address the following comments:

Line numbers are from the manuscript in the response from the authors.

We thank the Editor for this careful review of our manuscript. We have revised our manuscript following all his suggestions. Please, find the marked-up version of the manuscript at the end of this document.

L. 75: uncertainty -> uncertainties.

Done

L. 121: Perhaps introduce the acronym for "CHIMERE"?

To our knowledge, CHIMERE is an acronym, see Menut et al. (2013) and the CHIMERE webpage: <http://www.lmd.polytechnique.fr/chimere/>

L. 130-131: Perhaps consider removing the brackets and introducing a comma, thus: "...is weak, when...".

Done

L. 177: Suggest you do not start a sentence with an acronym. Thus, you could use "The OSSEs...".

Done

L. 181: Re-reading this, perhaps it would be better to have "In OSSEs, twin...".

Done

L. 195-198: Re-reading this, the sentence looks clumsy. Consider rewording thus: "...state-of-the-art set-up which solves the NEE...level of evaluation. This set-up includes a variational atmospheric inversion system and the ICOS23 network containing...years."

We have rephrased it a bit differently.

L. 212: this -> its.

Done

L. 217: "...developments of mesoscale...".

Done

L. 222: "...and of future...".

Done

L. 229: Do you need "state"?

Done

L. 246: "their typical estimate" -> "typical estimates".

Done

L. 267: I suggest "...typically distances less than 40km...".

Done

L. 273: measurements -> measurement.

Done

L. 277: I suggest "...the use of this assumption...".

Done

L. 297-298: I suggest "...is relatively large compared to the typical...sites, due to atmospheric diffusion.".

Done

L. 323: To break the very long sentence I suggest: "...The operator H: ...".

Done.

L. 326: I suggest "The operator H is the combination...".

Done

L. 343: averages -> averaged.

Done

L. 353, 378: I suggest you remove "below".

Done

L. 359: Do you mean: "..., as done in Hungershoefer et al. (2010)..."?

Done

L. 377: I suggest you use "e.g." instead of "i.e.".

Done

L. 390-391: "...by the ECMWF analyses.".

Done

L. 415: I suggest you omit "respectively".

Done

L. 442: What two types of correlations? In space and time?

We have clarified it

L. 445: I suggest you omit "to".

Done

L. 448: proportionally -> proportional.

Done

L. 448-449: Clarify the statement in brackets – I do not understand what you mean.

Done

L. 451: Would this be better?: "...summer, providing typical values for...errors of...".

Done

L. 473: constrain -> constraint.

Done

L. 498: seems-> is; I suggest: "may confirm" -> "suggests".

Done

L. 503: Not clear on the reference to Broquet. Is this result discussed in this paper, or are the hourly averages provided by Broquet? Please clarify.

We have clarified it

L. 509: dimensions -> dimension.

Done

L. 640 Do you mean "western European" countries and "eastern European" countries? If so, please clarify.

Done

L. 657: "national scale".

Done

L. 659: Omit "the".

Done

L. 664: chose -> choose.

Done

L. 685: "...and much larger...".

Done

L. 704, 714: "...the whole of Europe...".

Done

L. 743: I suggest you remove "even".

Done

L. 762-763: Reword this sentence – I do not understand it.

We have removed it since the diversity of the results is already illustrated with the other examples.

L. 785: I suggest "decreases" -> "reductions"; perhaps: critical -> important?

Done

L. 811: Not clear whether the 64-67% refers to the relatively constant increase, or to values that are smaller by this amount. Please reword.

We have clarified it

L. 819: As this is the synthesis section, I suggest you indicate that you consider here northern summer and northern winter.

Done

L. 839: I suggest: "...promising for provision of accurate monitoring of the NEE...".
Done

L. 851: Remove "such".
Done

L. 872: "..., respectively".
Done

L. 880: "...than those in the...".
Done

L. 882: What is this target? Please indicate.
Done

L. 893: reaching it -> to reach it.
Done

L. 897: I suggest: depending -> which depends.
Done

L. 900: "...western European countries...".
Done

L. 909: I suggest "...European network..."; it -> its.
Done

L. 915: "...the increase in the size of the network...".
Done

L. 916: Perhaps "accuracy" is better than "precision"?
Done

L. 951-952: "...results in very slight increases...".
Done

L. 952: differences in what?
We remove it since the meaning of this parenthesis was similar to that of "slight".

L. 954: alter -> changes; "...only for specific areas...".
Done

L. 976-977: I suggest: "...Broquet et al. (2013), but only at the European scale.".
Done

L. 1403: In Fig. 5, the crosses are difficult to see. Consider increasing their size.
Done

Reference:

Menut, L., Bessagnet, B., Khvorostyanov, D., Beekmann, M., Blond, N., Colette, A., Coll, I., Curci, G., Foret, G., Hodzic, A., Mailler, S., Meleux, F., Monge, J.-L., Pison, I., Siour, G., Turquety, S., Valari, M., Vautard, R., and Vivanco, M. G.: CHIMERE 2013: a model for regional atmospheric composition modelling, *Geosci. Model Dev.*, 6, 981-1028, doi:10.5194/gmd-6-981-2013, 2013.

On the potential of ICOS atmospheric CO₂ measurement network for the estimation of the biogenic CO₂ budget of Europe

N. Kadygrov¹, G. Broquet¹, F. Chevallier¹, L. Rivier¹, C. Gerbig² and P. Ciais¹

¹ Laboratoire des Sciences du Climat et de l'Environnement, CEA-CNRS-UVSQ, 91191, Gif sur Yvette Cedex, France

² Max Planck Institute for Biogeochemistry, Jena, Germany

Correspondence to: N. Kadygrov (kadygrov@gmail.com)

Abstract

We present a performance assessment of the European Integrated Carbon Observing System (ICOS) atmospheric network for constraining European biogenic CO₂ fluxes (hereafter Net Ecosystem Exchange, NEE). The performance of the network is assessed in terms of uncertainty in the fluxes using a state-of-the-art mesoscale variational atmospheric inversion system assimilating hourly averages of atmospheric data to solve for NEE at 6 hour and 0.5° resolution. The performance of the ICOS atmospheric network is also assessed in terms of uncertainty reduction compared to typical uncertainties in the flux estimates from ecosystem models that are used as prior information by the inversion. The uncertainty in inverted fluxes is computed for two typical periods representative of northern summer and winter conditions in July and in December 2007, respectively. These computations are based on a Observing System Simulation Experiment (OSSE) framework. We analyze the uncertainty in two-week mean NEE as a function of the spatial scale, with a focus on the model native grid scale (0.5°), the country scale and the European scale (including western Russia and Turkey). Several network configurations, going from 23 to 66 sites, and different configurations of the prior uncertainties and atmospheric model transport errors are tested in order to assess and compare the improvements that can be expected in the future from the extension of the network, from improved prior information or transport models. Assimilating data from 23 sites (a network comparable to present day capability) with errors estimated from the present prior information and transport models, the uncertainty reduction on two-week mean NEE should range between 20% and 50% for 0.5° resolution grid cells in the best sampled area encompassing eastern France and western Germany. At the European scale, the prior uncertainty in two-week mean NEE is reduced by 50% (66%), down to ~ 43 TgCmonth⁻¹ (26 TgCmonth⁻¹) in July (December). Using a larger network of 66 stations, the prior uncertainty of NEE is reduced by the inversion by 64% (down to ~33 TgC month⁻¹) in July and by 79% (down to ~15 TgC month⁻¹) in December. When the results are integrated over the well-observed western European domain, the uncertainty reduction

shows no seasonal variability. The effect of decreasing the correlation length of the prior uncertainty, or of reducing the transport model errors compared to their present configuration (when conducting real-data inversion cases) can be larger than that of the extension of the measurement network in areas where the 23 stations observation network is the densest. We show that with a configuration of the ICOS atmospheric network containing 66 sites that can be expected on the long-term, the uncertainties in two-week mean NEE will be reduced by up to 50-80 % for countries like Finland, Germany, France and Spain, which could bring a significant improvement of (and at least a high complementarity to) our knowledge about NEE derived from biomass and soil carbon inventories at multi-annual scales.

1 Introduction

Accurate information about the terrestrial biogenic CO₂ fluxes (hereafter Net Ecosystem Exchange - NEE) is needed at the regional scale to understand the drivers of the carbon cycle (Ciais et al., 2014). Accounting for the natural fluxes in political agreements regarding the reduction of the CO₂ emissions requires their accurate quantification over administrative areas, and in particular over countries and smaller regional scales at which land management decisions can be implemented.

Atmospheric inversions, which exploit atmospheric CO₂ mole fraction measurements to infer information about surface CO₂ fluxes (Enting, 2002) are expected to deliver robust and objective quantification of NEE at high temporal and spatial resolution over continuous areas and time periods. Global atmospheric inversions have been widely used to document natural carbon sources and sinks (Gurney et al., 2002, Rodenbeck et al., 2003). However, the spread of the results from the different global inversion studies and the diagnostics by some of these studies demonstrate that the uncertainties remain large at the one month and continental scale (Peylin et al., 2013). Such large uncertainties are mainly due to the lack of observations over the continents

Deleted: uncertainty

or to the limited ability of global systems to account for dense observation networks in addition to errors in large-scale atmospheric transport models. However, with an increasing number of continuous atmospheric CO₂ observations, primarily in North America and Europe, and with the development of regional inversion systems using high resolution mesoscale atmospheric transport models and solving for NEE at typical resolutions of 10 to 50 km (Lauvaux et al., 2008, 2012, Schuh et al., 2010, Broquet et al., 2011, Meesters et al., 2012), there is an increasing ability to constrain NEE at continental to regional scales.

This paper aims at studying the skill of a regional inversion system in Europe, which is equipped with a relatively large number of ground-based atmospheric measurement stations, for estimating NEE at the continental and country scales, down to 0.5° resolution (which is the resolution of the transport model used in the inversion system). It also aims at assessing and comparing the benefits from the measurement network extensions and from future improvement in the inversion system. Such improvement can be anticipated either due to better atmospheric transport models or to the use of better flux estimates as the prior information that gets updated by the inversion based on the assimilation of atmospheric measurements.

Europe is a difficult application area for atmospheric inversion because of the very heterogeneous distribution of vegetation types, land use, and agricultural and industrial activities inside a relatively small domain, and, consequently, because of the need for solving for fluxes at high resolution. Furthermore, its complex terrain also requires a high resolution of the topography when modeling the atmospheric transport (Ahmadov et al., 2009). However, the Integrated Carbon Observing System (ICOS) infrastructure is setting up a dense network of standardized, long-term, continuous and high precision atmospheric and flux measurements in Europe, with the aim of understanding the European carbon balance and monitoring the effectiveness of Greenhouse Gas (GHG) mitigation activities (<http://www.icos-infrastructure.eu/>). The atmospheric network is expected to increase from an initial configuration

of around 23 stations where actual measurements have been conducted during the past five years (even though all these sites will not necessarily be included in the official ICOS network in the coming years) up to around 60 stations in the near future (see ICOS Stakeholder handbook 2013 at https://icos-atc.lsce.ipsl.fr/?q=doc_public). In this context, the developers of the ICOS atmospheric network have encouraged network assessment studies such as the one conducted in this paper.

Several inversion studies have focused on the estimate of European NEE based on measurements from the CarboEurope-IP atmospheric stations, most of which are planning to join the ICOS atmospheric network (Peters et al., 2010, Broquet et al., 2011). Broquet et al. (2013) have demonstrated, based on comparisons with independent flux tower measurements, that there is a high confidence in the Bayesian estimate of the European NEE and of its uncertainty at the 1-month and continental scale based on their variational system which uses the CHIMERE mesoscale transport model run at 0.5° resolution. The distributions of the misfits between 1 month and continental scale averages of the flux measurements and of the NEE estimates sampled at the flux measurement locations were shown to be unbiased and consistent with the estimate of the uncertainties from the inversion system. This gives confidence in the inversion configuration of Broquet et al. (2011, 2013) for the estimation of the performance of the ICOS network. In particular, it gives confidence in their assumptions that the distribution of the uncertainties are unbiased and Gaussian, and that the impact of the uncertainties in the CO₂ modeling domain boundary conditions at the edges of Europe, and in the CO₂ fossil fuel emissions is weak when assimilating measurements from the type of sites that form the ICOS network.

Here, we apply the system of Broquet et al. (2011, 2013) to assess the potential of the near term and realistic future configurations of the ICOS continuous measurements of CO₂ dry air mole fraction to improve NEE estimates at the mesoscale across Europe. This assessment is based on a

Deleted: (

Deleted:).

126 quantitative evaluation of the uncertainties in the inverted fluxes (also called posterior
 127 uncertainties) which are compared to the uncertainties in the prior information on NEE used by
 128 the inversion system.

129 The Bayesian statistical framework chosen here provides estimates of the posterior uncertainties
 130 as a function of the prior uncertainties, of the atmospheric transport and of the combination of
 131 statistical errors which are not controlled by the update of the prior NEE by the inversion (like
 132 the measurement errors and the atmospheric transport errors). Even though the prior uncertainty
 133 can potentially depend on the value of the prior NEE, the actual values of the prior NEE or of the
 134 measurement data to be assimilated are not formally involved in the estimation of the posterior
 135 uncertainty due to the linearity of the atmospheric transport of CO₂. Therefore, the posterior
 136 uncertainty can be derived for hypothetical observation networks or for hypothetical
 137 uncertainties in the prior information or from the atmospheric transport model (i.e., for
 138 hypothetical improvements in the prior information or in the atmospheric transport model) using
 139 an Observing System Simulation Experiment (OSSE) framework, in which the results do not
 140 depend on a simulated truth. Due to the dimension of the problem, uncertainties are not derived
 141 analytically in this study and we use a Monte Carlo ensemble approach.

142 Using synthetic data in an OSSE framework has been a common way to assess the utility of new
 143 GHG observing systems for the monitoring of the GHG sources and sinks at large scales based
 144 on global inversion systems with coarse resolution transport models (e.g., Rayner et al., 1996,
 145 Houweling et al., 2004, Chevallier et al., 2007, Kadyrov et al., 2009, Hungershofer et al.,
 146 2010). This approach now plays a critical role in the recent emergence of regional inversion
 147 systems supporting strategies for the deployment of regional observation networks and assessing
 148 the potential of regional inversion for assessing the GHG fluxes at a relatively high resolution
 149 (Tolk et al., 2011, Ziehn et al., 2014). Such a use of OSSEs today is not specific to the GHG
 150 inversion community. [The](#) OSSEs are increasingly used by the air quality community (e.g.,

151 Edwards et al., 2009, Timmermans et al. 2009a, b, 2015, Claeyman et al., 2011) and they are
152 still extensively used by the meteorological community (e.g., Masutani et al., 2010, Riishøjgaard
153 et al., 2012, Errico et al., 2013, see also [https://www.gmes-](https://www.gmes-atmosphere.eu/events/osse_workshop/)
154 [atmosphere.eu/events/osse_workshop/](https://www.gmes-atmosphere.eu/events/osse_workshop/)).

155 In OSSEs, twin experiments are often used to derive a single realization of the uncertainties
156 (Masutani et al., 2010) while our Monte Carlo approach explores the uncertainty space much
157 more extensively. Further, in common (linear) CO₂ atmospheric inversions, since the results are
158 independent of the synthetic “true” data used for the OSSE, any simulation can be used to build
159 this truth, while, when using fraternal twin experiments with nonlinear models in other
160 application fields of data assimilation, it is critical to ensure that the truth is realistic enough
161 (Halliwell et al., 2014). The reliability of the OSSEs in CO₂ atmospheric inversion critically
162 depends on the realism of their input error statistics since their configuration in the inversion
163 system is perfectly consistent with the sampling of synthetic errors that are used in these
164 experiments. In this study, our confidence in the realism of the statistical modeling approach and
165 of the input error statistics, and thus in the inversion set-up, is based on the statistical modeling
166 studies of Chevallier et al. (2012) and Broquet et al. (2013) that were themselves based on real
167 data.

168 The manuscript first documents the potential of different configurations of the ICOS network for
169 constraining NEE, through the use of a state-of-the-art inversion set-up which solves the NEE at
170 high spatial and temporal resolution, and which has been submitted to a high level of evaluation.
171 This inversion set-up is based on variational atmospheric inversion system. We study the
172 potential of the ICOS23 network containing existing sites and other stations that could be
173 installed on tall towers over Europe in the coming years. We also consider two longer-term
174 ICOS configurations with 50 stations (hereafter ICOS50) and 66 stations (hereafter ICOS66).
175 For the time domain, we consider results for NEE aggregated at the two-week scale, for two

Deleted: these areas

Deleted: , i.e.,

Deleted: ,

Deleted: , and

Deleted: the ICOS23

181 different periods of the year (in July and in December). Shorter aggregation scales, like a day,
182 result in a significant dependency of NEE to specific synoptic events. Longer time scales require
183 computing resources that are beyond the scope of this study with ~~its~~ high-resolution inversion
184 system. We pay special attention to the analysis of the results at different spatial scales, from the
185 native transport model grid scale of about 50x50 km² up to the national scale that is the most
186 relevant for supporting environmental policy, and the full European domain considered in this
187 study (which extends to western Russia and Turkey). We also present the sensitivity of our
188 results to parameters characterizing the future developments of mesoscale inversion systems: the
189 reduction of the transport model errors or of the prior flux errors.

Deleted: this

Deleted: the

190 The paper is organized as follows. Section 2 describes the mesoscale inversion experimental
191 framework focusing on the Monte Carlo estimate of uncertainties. Section 3 analyses the scores
192 of posterior uncertainties and the uncertainty reduction compared to the prior uncertainties in
193 order to assess the potential of the near term framework and ~~of future improvements of the~~
194 network or of the inversion set-up. The last section synthesizes the results and discusses them.

Deleted: the one

195

196 2 Materials and Methods

197 2.1 The configurations of the ICOS atmospheric observation network

198 We consider three successive phases of deployment of the ICOS atmospheric network. The
199 initial ~~ICOS23~~ configuration includes 23 sites among which there are eight tall towers. This
200 minimum network configuration is based on existing stations, most of them being operational in
201 the CarboEurope-IP FP6 project. The ICOS network is expected to further expand during the
202 next 5 years according to the country declarations at the ICOS Interim Stakeholder Council and
203 to the ICOS European Research Infrastructure Consortium 5 year financial plan. Using possible
204 locations for the future stations, including sites that have already been discussed with the ICOS

Deleted: state

209 consortium during the ICOS preparatory phase FP7 project (European Union's Seventh Research
210 Framework Programme, grant agreement No. 211574), we derived two plausible ICOS
211 configurations: ICOS50 with 50 sites including 24 tall towers and ICOS66 with 66 sites
212 including 33 tall towers.

213 The locations and details on the sites of the three configurations are summarized in Table A1 and
214 in Fig. 1. Here, the existing and future ICOS CO₂ observations are assumed to comply with the
215 World Meteorological Organization (WMO) accuracy targets of 0.1 parts per million (ppm)
216 measurement precision (WMO, 1981, Francey, 1998) so that the measurement error is negligible
217 in comparison to the other type of errors that have to be accounted for in the inversion
218 framework such as the model transport and representation errors (see their typical estimates in
219 Sect. 2.2.2).

Deleted: estimate

220

221 2.2 Mesoscale inversion system

222 2.2.1 Method

223 The estimate of uncertainties related to the different ICOS networks is based on an ensemble of
224 inversions with the variational inversion system of Broquet et al. (2011), assimilating synthetic
225 hourly averages of the atmospheric CO₂ data from these networks (during the afternoon or
226 during nighttime only, depending on the type of sites that are considered, see Sect. 2.2.2.). A
227 regional atmospheric transport model (see its description below) is used to estimate the
228 relationship between the CO₂ fluxes and the CO₂ mixing ratios. The inversion system solves for
229 6-hour mean NEE on each grid point of the 0.5° by 0.5° resolution grid used for the transport
230 modeling. It also solves for 6-hour mean ocean fluxes at 0.5° spatial resolution in order to
231 account for errors from air-sea fluxes when mapping fluxes into hourly mean mixing ratios.
232 However, analyzing the uncertainty reduction for ocean fluxes is out of the scope of this paper.

234 Peylin et al. (2011) indicate that uncertainties in anthropogenic fluxes yield errors when
235 simulating CO₂ mixing ratios at ICOS stations that are smaller than atmospheric model errors.
236 Furthermore, the relative uncertainty in anthropogenic emissions is smaller than that in NEE,
237 while on short timescales, the anthropogenic signal is generally smaller than the signature of the
238 NEE at sites that are not very close (typically ~~distances~~ less than 40km) to strong anthropogenic
239 sources such as cities (see the analysis for the Trainou ICOS station near Orléans, in France by
240 Bréon et al. 2015). Relying on such indications, we assume that the errors due to uncertainties in
241 anthropogenic emissions are negligible compared to errors from NEE and atmospheric model
242 errors. This is a reasonable assumption as long as most ICOS stations are relatively far from
243 large urban areas, which should be the case since the ICOS atmospheric station specification
244 document (https://icos-atc.lsce.ipsl.fr/?q=doc_public) recommends that the ~~measurement~~ sites
245 are located at more than 40km from the strong anthropogenic sources (such as the cities). Zhang
246 et al. (2015) yield conclusions from their transport experiments at 1° resolution which contradict
247 this assumption and this clearly raises an open debate. However, the evaluation of the inversion
248 configuration from Broquet et al. (2013) supports ~~the~~ use of this assumption for our study.
249 In order to simulate the full amount of CO₂ in the atmosphere, the inversion uses a fixed estimate
250 of the fossil fuel emissions (see below) without attempting to correct it nor account for
251 uncertainties in these fluxes. The inversion also uses a fixed estimate of the CO₂ boundary
252 conditions at the lateral and top boundaries of the regional modeling domain without attempting
253 to correct it nor account for uncertainties in these conditions. This follows the protocol from
254 Broquet et al. (2011) which assumed that the error from the boundary conditions for the
255 European domain is mainly a bias and which corrects for such a bias in a preliminary step that is
256 independent to the subsequent application of the inversion. Such an assumption is supported by
257 the evaluation of the inversion configuration by Broquet et al. (2013). The relatively weak
258 impact of uncertainties in the boundary conditions in Europe (while studies in other regions such
259 as that of Gockede et al. (2010) indicate a high influence of such uncertainties) can be explained

Deleted: at

Deleted: measurements

Deleted: our

263 by the fact that the spatial scale of the incoming CO₂ patterns at the ICOS sites from remote
 264 sources and sinks outside the European domain boundaries is relatively large compared to the
 265 typical distances between the ICOS sites, due to atmospheric diffusion (especially under west
 266 wind conditions, when the air comes from the Atlantic ocean). In principle, the inversion mainly
 267 exploits the smaller scale signal of the gradients between the sites to constrain the NEE, and it is
 268 thus weakly influenced by the large scale signature of the uncertainty in the boundary conditions.
 269 In this section we only summarize the main elements of the inversion system, starting with the
 270 theoretical framework, while the detailed description can be found in Broquet et al. (2011).

271 We define the control vector \mathbf{x} of the atmospheric inversion as the 6-hour and 0.5°x0.5° mean
 272 NEE and ocean fluxes. The atmospheric inversion seeks the mean \mathbf{x}_a and covariance matrix \mathbf{A} of
 273 the normal distribution $N(\mathbf{x}_a, \mathbf{A})$ of the knowledge on \mathbf{x} based on (i) the atmospheric transport
 274 model, (ii) the prior knowledge \mathbf{x}_b of \mathbf{x} , (iii) the hourly mean atmospheric measurements \mathbf{y} , (iv
 275 and v) the covariances \mathbf{B} and \mathbf{R} of the distributions of the prior uncertainty and of the
 276 observation error assuming that these uncertainties are normal and unbiased (i.e., equal to $N(0,$
 277 $\mathbf{B})$ and $N(0, \mathbf{R})$ respectively), and (vi) a Bayesian relationship between these distributions. The
 278 observation error is the combination of all sources of misfit between the atmospheric transport
 279 model and the concentration measurements other than the prior uncertainty, in particular the
 280 measurement errors, the model transport, aggregation and representation errors, and the errors
 281 from the model inputs that are not controlled by the inversion.

282 With this theoretical framework, \mathbf{x}_a is the minimum of the quadratic cost function $J(\mathbf{x})$ (Rodgers,
 283 2000):

$$284 \quad J(\mathbf{x}) = \frac{1}{2}(\mathbf{x} - \mathbf{x}_b)^T \mathbf{B}^{-1}(\mathbf{x} - \mathbf{x}_b) + \frac{1}{2}(H(\mathbf{x}) - \mathbf{y})^T \mathbf{R}^{-1}(H(\mathbf{x}) - \mathbf{y}) \quad (1)$$

285 where ^T denotes the transpose, and where H is the affine observation operator which maps the 6-
 286 hour (00:00-06:00, 06:00-12:00, 12:00-18:00 and 18:00-24:00; UTC time is used hereafter) and

Deleted:) compared to the typical distances between the ICOS sites.

289 $0.5^\circ \times 0.5^\circ$ mean NEE and ocean CO_2 fluxes \mathbf{x} to the observational space based on the linear
 290 CO_2 atmospheric transport model with fixed open boundary conditions, and with fixed estimates
 291 of the anthropogenic fluxes and natural fluxes at resolutions higher than 6-hour and 0.5° . The
 292 operator $H: \mathbf{x} \rightarrow H(\mathbf{x})$ can be rewritten $H: \mathbf{x} \rightarrow \mathbf{H}\mathbf{x} + \mathbf{y}_{\text{fixed}}$ where $\mathbf{y}_{\text{fixed}}$ is the signature, through
 293 atmospheric transport, of the fluxes (in particular the anthropogenic emissions) and boundary
 294 conditions not controlled by the inversion. The operator \mathbf{H} is the combination of two linear
 295 operators: the first operator distributing 6-hour mean natural fluxes at the 1-hour resolution, and
 296 the second operator simulating the atmospheric transport from the 1-hour resolution fluxes at
 297 0.5° resolution.

298 The inversion system derives an estimate of \mathbf{x}_a by performing an iterative minimization of $J(\mathbf{x})$
 299 with the M1QN3 algorithm of Gilbert and Lemaréchal (1989). The gradient of J is derived using
 300 the adjoint operator of \mathbf{H} thanks to the availability of the adjoint version of the CHIMERE code.
 301 The covariance of the posterior uncertainty in inverted NEE \mathbf{A} , of main interest for this study, is
 302 given by the formula:

$$303 \quad \mathbf{A} = (\mathbf{B}^{-1} + \mathbf{H}^T \mathbf{R}^{-1} \mathbf{H})^{-1} \quad (2)$$

304 This equation demonstrates the point raised in the introduction for justifying the OSSE
 305 framework, that \mathbf{A} does not depend on the observations or on the prior flux values themselves
 306 but only on their error covariance matrices, on the observation network density and station
 307 location, and on the atmospheric transport operator. This allows assessing the performance of
 308 any observation system, whether existing or not. Of note is also that this calculation does not
 309 depend on $\mathbf{y}_{\text{fixed}}$, i.e., on the boundary conditions or on the anthropogenic fluxes in the domain so
 310 that such components can be ignored for the estimate of \mathbf{A} .

311 In this framework, a common performance indicator is the theoretical uncertainty reduction for
 312 specific budgets of the NEE estimates (averaged over specified periods of time and over
 313 specified spatial domains), defined by:

Deleted: °;

Deleted: averages

316
$$\gamma = 1 - \frac{\sigma_a}{\sigma_b} \quad (3)$$

317 where σ_a and σ_b are the standard deviations of the posterior and prior uncertainties in the
 318 corresponding integrals in time and space (over the given periods of time and spatial domains) of
 319 the 6-hour and 0.5° resolution NEE field. If the observations perfectly constrain the inversion of
 320 a given budget of NEE, then $\gamma = 1$. If the observations do not bring any information to reduce the
 321 error from the prior, $\gamma = 0$. By definition, γ is a quantity relative to the uncertainty in the prior
 322 fluxes, which depends on the type of prior information on NEE that is expected to be used
 323 (estimates from a biosphere model in our case, see Sect. 2.2.2). Of note is that the scores of
 324 uncertainty and of uncertainty reduction given in this study refer to the standard deviation of the
 325 uncertainty in a specific budget of NEE, and that, hereafter, the term “standard deviation” is
 326 generally omitted.

327 Due to the size of the observation and control vectors in this study, we could not afford the
 328 analytical computation of Eq. (2) based on the full computation of the \mathbf{H} matrix (using a very
 329 large number of transport simulations, as done in Hungershoefer et al. (2010). Instead we use the
 330 Monte Carlo approach of Chevallier et al. (2007) to compute \mathbf{A} . In this approach, an ensemble of
 331 posterior fluxes \mathbf{x}_{ai} is derived from an ensemble of inversions using the synthetic prior flux \mathbf{x}_{bi}
 332 and data \mathbf{y}_i whose random errors ($\mathbf{x}_{bi} - \mathbf{x}_{true}$ for \mathbf{x}_{bi} and $\mathbf{y}_i - \mathbf{H}\mathbf{x}_{true}$ for \mathbf{y}_i) with respect to a known truth
 333 (\mathbf{x}_{true} , whose value does not influence the results analyzed here, and which is thus ignored
 334 hereafter) sample the distributions $\mathcal{N}(0, \mathbf{B})$ and $\mathcal{N}(0, \mathbf{R})$. \mathbf{A} is obtained as the statistics of the
 335 posterior errors $\mathbf{x}_{ai} - \mathbf{x}_{true}$. The practical size of the ensemble is described below and its
 336 determination follows the discussion by Broquet et al. (2011). The convergence of the estimate
 337 of the inverted NEE for each inversion and the convergence of the statistics of the ensemble are
 338 necessary to ensure that the \mathbf{A} matrix computed with this method corresponds to the actual
 339 covariance of the posterior uncertainty given by Eq. (2). These convergences cannot be perfect
 340 with a limited number of iterations for the minimization algorithm and a limited number of

Deleted: below

Deleted: ,

Deleted: CHIMERE

Deleted: ;

345 inversion experiments in the Monte Carlo ensemble imposed by computational limitations.

346 Therefore the estimate of **A** can depend on parameters other than **H**, **B** and **R** in practice, e.g., the
347 number of iterations and of inversion experiments. However, it has been checked (see Sect.
348 2.2.2) that the convergence is sufficient so that this dependence should not be significant for the
349 quantities of interest.

350

351 2.2.2 Practical set-up

352 Atmospheric transport model

353 In this study, the operator **H** is based on the CHIMERE mesoscale atmospheric transport model
354 (Schmidt et al., 2001) forced with European Centre for Medium-Range Weather Forecasts
355 (ECMWF) winds. We use a configuration with a 0.5°x0.5° horizontal grid and with 25 σ -
356 coordinate vertical levels starting from the surface and with a ceiling at ~500 hPa (such a ceiling
357 being usual for regional transport modeling when focusing on mole fractions close to the ground,
358 e.g. Marécal et al. 2015). The spatial extent of the corresponding domain is described below.
359 CHIMERE is an off-line transport model. Hourly mass-fluxes are provided by the [ECMWF](#)
360 analyses. The relatively high vertical and horizontal resolutions of CHIMERE allow a good
361 vertical discretization of the Planetary Boundary Layer (PBL; the first 14 levels are below 1500
362 meters) along with a good representation of the orography and dynamics to match high
363 frequency observations better than with a global configuration whose typical horizontal
364 resolution is ~3° (Peylin et al. 2013).

365

366 Spatial and temporal domains

367 In this study, we use the European domain shown in Fig. 1a which covers most of the European
368 Union and some of Eastern Europe, with a land surface area of $6.8 \times 10^6 \text{ km}^2$. Its southwest corner

Deleted: i.

Deleted: below

Deleted: of the ECMWF

is at 35°N and 15°W, and its northeast corner is at 70°N and 35°E. Two temporal windows are considered, from June 30, 2007 to July 20, 2007 and from 2 to 22 of December 2007 (of almost three weeks each). The choice of these periods of three weeks is a tradeoff between widening the scope of the study and computational burden. The Monte Carlo-based flux uncertainty reduction calculations require large computing resources, while we test three different network configurations for two different months, and for different setups of the error covariance matrices. Three week experiments allow retrieving information about uncertainties at the two-week scale without being biased by edge effects, i.e., they allow accounting for the impact of uncertainties from the days before the 14 targeted days and for the impact of the assimilation of measurements during the days after these 14 targeted days. The advection of CO₂ throughout Europe can last more than three days, but atmospheric diffusion ensures that the signature at ICOS sites of the NEE during a 6-hour window is generally negligible after three days of transport (not shown).

Thus, the windows 3-17 July and 5-19 December were chosen for analysis. We consider the results for July and December to be representative for the summer and winter seasons (using the name of the seasons for the Northern Hemisphere hereafter), allowing an analysis of seasonal variations of the flux uncertainty reduction. Choosing year 2007 for the period of the inversion only impacts the meteorological conditions (i.e., the impact on the prior uncertainty whose local standard deviations are scaled using data from this specific year, as detailed below in this section, is negligible) and thus the atmospheric transport conditions in the OSSEs. We assume that these conditions are not impacted by a strong inter-annual anomaly in 2007 so that they can be expected to be representative of average conditions for summer and winter. Hereafter, the mention of the year 2007 is thus often ignored and we assume that we retrieve typical estimates for July and December.

Deleted: respectively.

Flux error covariance matrix

398 The set-up of the error covariance matrix **B** follows the methodology of Chevallier et al. (2007).
 399 It is chosen to represent the typical uncertainty in estimates from the biosphere models (for NEE)
 400 and from climatologies (for ocean fluxes) used by traditional atmospheric inversion systems. The
 401 statistics have been derived for estimates from the Organising Carbon and Hydrology In
 402 Dynamic Ecosystems (ORCHIDEE) vegetation model (Krinner et al., 2005) and the ocean
 403 climatology from Takahashi et al. (2009). The uncertainties in NEE are assumed to be
 404 autocorrelated in space and in time and are modeled using isotropic and exponentially decreasing
 405 functions with correlation lengths that do not depend on the time or location. A Kronecker
 406 product of the matrices of temporal and spatial correlations is applied to define the correlations
 407 between uncertainties for different locations and time windows. The e-folding spatial and
 408 temporal correlation lengths are set according to the estimation of Chevallier et al. (2012) based
 409 on comparison of the NEE derived by the ORCHIDEE model and eddy-covariance flux tower
 410 data, for our specific prior flux spatial and temporal resolution, i.e., 30 days in time and 250 km
 411 in space over land. NEE uncertainties for different 6-hour windows of the day are not correlated,
 412 i.e., the temporal correlations only apply to a given 6-hour window of consecutive days. The
 413 standard deviations of the prior uncertainties in **B** are set proportional to the heterotrophic
 414 respiration fluxes from the ORCHIDEE model (the corresponding proportional coefficient
 415 between the heterotrophic respiration and the prior uncertainty at the daily and 0.5° scale is
 416 approximately 2). We apply time-dependent scaling factors to these fluxes so that the NEE
 417 uncertainties have lower values during the night than during the day, and during winter than
 418 during summer, providing typical values for grid-scale and daily errors of $\sim 2.5 \text{ gCm}^{-2}\text{day}^{-1}$ in
 419 summer (maximum value $3.4 \text{ gCm}^{-2}\text{day}^{-1}$) and of $\sim 2 \text{ gCm}^{-2}\text{day}^{-1}$ in winter (maximum value 3.1
 420 $\text{gCm}^{-2}\text{day}^{-1}$). Over the ocean, the prior uncertainty of air-sea fluxes has standard deviations at the
 421 0.5° and 6-hour scale equal to $0.2 \text{ gCm}^{-2}\text{day}^{-1}$, an e-folding spatial correlation length of 500 km
 422 and temporal correlations similar to those for the prior uncertainties over land. Prior ocean and
 423 land flux uncertainties are not correlated.

Deleted: ensures

Deleted: combination of these two types of

Deleted: .

Deleted: to

Deleted: proportionally

Deleted: it is approximately twice this

Deleted: summing up to

432

433 **Time selection of the data to be assimilated**

434 Broquet et al. (2011) analyzed the periods of time during which the CHIMERE European
435 configuration bears transport biases which are too high so that measurements from ground based
436 stations such as ICOS sites should not be assimilated to avoid projecting erroneously such biases
437 into the corrections to the fluxes. In agreement with common practice, they concluded that
438 observations at low altitude sites (approximately below 1000 meters above sea level (masl); see
439 Broquet et al. (2011) for the exact definition of the different types of sites used for the time
440 selection of the data and the configuration of the observation error) which include almost all of
441 the ICOS tall towers, should be assimilated during daytime (12:00-20:00) while the observations
442 at high altitude stations (approximately above 1000 masl) should be used during the night
443 (00:00-06:00) only. This generally yields larger uncertainty reduction during daytime than
444 during nighttime (Broquet et al. 2011). However, this does not raise a potential bias related to a
445 better constraint on daytime inverted NEE (when the ecosystems are generally a sink of CO₂)
446 than on nighttime inverted NEE (when the ecosystems are generally a source of CO₂) since
447 uncertainties in both nighttime and daytime prior NEE, transport and measurements are assumed
448 to be unbiased, as supported by the results from Broquet et al. (2013).

Deleted: constrain

449

450 **Observation error covariance matrix**

451 The observational error covariance matrix **R** accounts for various sources of error when
452 comparing the hourly data selected for assimilation and their simulation which are not controlled
453 by the inversion: measurement error, aggregation error, atmospheric model representativeness
454 and transport error (as explained previously, uncertainties in the anthropogenic emissions and in
455 the boundary conditions are assumed to be negligible). The first two terms are negligible

457 compared to the model representativeness and transport error due to the high measurement
 458 standard and to solving for the fluxes at 6-hour and 0.5° resolution during the inversion,
 459 respectively.

460 Broquet et al. (2011) derived a quantitative estimation of the model error (depending on the
 461 station height) including transport and representativeness errors based on comparisons between
 462 simulations and measurements of CO₂ and ²²²Rn during summer. Broquet et al. (2013) extended
 463 this analysis using 1-year long timeseries of simulated and measured CO₂ and ²²²Rn, to provide
 464 season-dependent estimates which are used here. The model error is much higher during the
 465 winter than that during the summer. It is given for each site in Table A1 for the two months
 466 (July, December) considered in this study. We assume that the errors for two different sites are
 467 independent and that they do not bear temporal autocorrelations. Thus, the observation error
 468 covariance matrix **R** is set diagonal. There is no evidence that such autocorrelations could be
 469 significant in the analysis of Broquet et al. (2011). The resulting budget of observation errors at
 470 daily to monthly resolution is reliable (Broquet et al. 2011, 2013). This suggests that the
 471 temporal auto-correlations of the actual observation errors are negligible. If the auto-correlations
 472 of the actual observation errors were not negligible, this would mean that the errors for hourly
 473 data are overestimated. In both cases, the assumption that the temporal autocorrelations of the
 474 observation error are negligible does not seem to need to be balanced by an artificial increase of
 475 the estimate of the observation errors for hourly averages provided by Broquet et al. (2013).
 476

Deleted: seems

Deleted: may confirm

Deleted: from

477 **Minimization and number of members in the Monte Carlo ensembles**

478 We use 12 iterations of minimization for each variational inversion of the Monte Carlo ensemble
 479 experiments. This number is similar to that from Broquet et al. (2011) where they considered a
 480 longer time period for the inversions but far smaller observation networks and a smaller
 481 inversion domain, which reduces the dimension of the minimization problem. However, here, 12

Deleted: dimensions

iterations were still found to be sufficient for converging toward the theoretical minimum of the cost function, i.e., the number of assimilated data divided by two (Weaver et al., 2003), with less than 10% relative difference to this theoretical minimum except for a few cases (for these cases, 18 iterations were used to reach a relative difference to the theoretical minimum that is smaller than 10%).

Similarly to Broquet et al. (2011), 60 members are used in each Monte Carlo ensemble experiment. This is also the typical number of members that Bousserez et al. (2015) use for their Monte Carlo simulations. Broquet et al. (2011) found a satisfactory convergence of the estimate of the uncertainties in Europe and 1-month average NEE with an ensemble size of 60, which is confirmed here (the estimates using 50 and more members are within 6% of the results with 60 members).

2.2.3 Sensitivity tests

Three and five Monte Carlo ensembles of inversions are conducted for December and July respectively. For each season, 3 ensembles using the default set-up of **B** and **R** described above are conducted in order to give results for the 3 different ICOS network configurations and consequently the sensitivity to the network configuration. In July, two ensembles are also conducted with a change in **R** in one case and in **B** in the other case in order to test the sensitivity to these inversion parameters. Such sensitivity tests have been conducted in July only and using one configuration of the ICOS network only (ICOS50 and ICOS66 for the test of sensitivity to **R** and **B** respectively) since a more exhaustive set of tests of sensitivity for the two seasons and for each ICOS network configuration was not expected to bring new insights while raising significant additional computation costs. The set-up of the inversion for these two sensitivity tests is now described.

510

511 **Test of the sensitivity to the observation error**

512 There is a steady increase in the resolution of the atmospheric transport models used for
513 atmospheric inversions, with corresponding improvements of the simulation precision (e.g., Law
514 et al. 2008). In this test we simulate the effect of potential future transport model improvement
515 on the posterior flux uncertainties by reducing the default observation error standard deviations
516 in \mathbf{R} by a factor of two. This factor roughly corresponds to the improvement of the misfits
517 between the model and actual measurement at the site TRN (see Fig. 1 for its location), that was
518 observed when bringing CHIMERE from the current 0.5° resolution down to a 2 km resolution
519 using the configuration presented in Bréon et al. (2014). The underlying assumption would be
520 that ~ 1 km horizontal resolution atmospheric transport models could be used for inversions at the
521 European scale in the near future. Hereafter, we denote by \mathbf{R}_{ref} the reference configuration of \mathbf{R}
522 and by \mathbf{R}_{red} the one corresponding to reduced standard deviations.

523

524 **Test of the sensitivity to the prior uncertainty**

525 The test of the sensitivity of the inversion system to the prior uncertainty is focused on that of the
526 sensitivity to the spatial correlation length in \mathbf{B} (Gerbig et. al. 2006) (which impacts the budget
527 of uncertainty over large regions). The possible use of better prior flux fields based on the
528 merging of both estimates from vegetation models and from large scale inventories (such as
529 forest and agricultural inventories) can be expected to generate smaller-scale uncertainties than
530 when using vegetation models while it is not obvious that local uncertainties would be decreased
531 when adding information from inventories (since inventories only measure long term integrated
532 NEE). Therefore, we tested the impact of reducing the spatial correlation length for the prior

uncertainty in NEE from 250 km to 150 km, denoting hereafter the corresponding configurations for the **B** matrix: **B**₂₅₀ and **B**₁₅₀ respectively.

3. Results and discussion

3.1 Assessment of the performance of the actual network and system

In this section, the performance of the inversion relying on the default configuration and on the ICOS23 initial state network (i.e., the reference inversion) is analyzed as a function of the spatial scale, highlighting the main patterns of the uncertainty reduction obtained from the pixel scale to the regional (national, European) scales.

3.1.1 Analysis at the model grid scale

Figures 2a and 2b show the uncertainty reduction for estimates of two-week average NEE at 0.5° resolution in July and December, respectively. This grid-scale uncertainty reduction reaches 65% for areas in the vicinity of the ICOS sites and decreases smoothly with distance away from measurement sites. For most of the area around eastern France – western Germany, this grid – scale uncertainty reduction ranges from 35 to 50% for July and from 20 to 40% for December. This stems from the combination of the dense observation network over that region, and from the 250 km correlation scale for the prior uncertainties, which spreads the error reduction beyond the immediate vicinity of each station where near field fluxes have a large influence on the mixing ratio at this station (Bocquet, 2005). For other parts of Europe that are not well sampled by ICOS, significant uncertainty reductions are generally seen around each site but there are large areas where the inversion has no impact at the grid scale: Scandinavian countries, the eastern part of Germany, Poland, the south of the Iberian Peninsula and almost all of Eastern Europe.

556 The spatial structure of the uncertainty reduction and the underlying spatial extrapolation from a
 557 site is a complex combination of transport influence and of the structure of the prior uncertainty.
 558 Due to varying transport conditions, standard deviation of the prior uncertainty at the grid scale
 559 (which is larger in summer, see below the comments on Fig. 3), and observation error (which is
 560 larger in winter), the spatial distribution of uncertainty reduction is found to vary from summer
 561 to winter. Because the prior uncertainties are larger and the observation errors are smaller in July
 562 than in December, there is generally a larger uncertainty reduction in July (especially in Western
 563 Europe). But variations in meteorology alter (limiting or enhancing) this general behavior. The
 564 lower vertical mixing (which strengthens the sensitivity of the near ground measurements to the
 565 local fluxes) partly balances the higher observation error in December and the range of local
 566 uncertainty reductions overlaps between July and December. The observations from the Angus
 567 tall tower (**tta** site, Table A1) in Scotland or from Pallas (**pal** site, Table A1) in Finland
 568 contribute differently to the uncertainty reduction during July and December (using
 569 meteorological conditions from 2007), showing better performance at the grid scale during
 570 summer. This also comes from the different weather regimes, with different dominant wind
 571 directions, different average wind speed and different vertical mixing in summer and winter.
 572 Regions lacking stations in ICOS23 have an uncertainty reduction which is more sensitive to the
 573 atmospheric transport than regions with a dense network. The uncertainty reduction in December
 574 is significantly larger in the east and in the southeast part of domain compared to July, due to
 575 more occurrences of winds from the east during December than during July.

576 Complementing the uncertainty reduction, Fig. 3 shows prior and posterior uncertainty standard
 577 deviations at the grid scale in order to illustrate the precision of the estimates of NEE that should
 578 be achievable with the reference inversion using the ICOS23 network. As already stated, prior
 579 uncertainties are up to $\sim 3 \text{ gCm}^{-2}\text{day}^{-1}$ (Fig. 3a) but the winter values are smaller than the summer
 580 ones (due to a weaker activity of the ecosystems; Fig. 3b). During both July and December, the
 581 uncertainties in two-week mean NEE in the regions that are best covered by observations (most

of Western Europe) at 0.5° resolution are reduced by the inversion down to typical values of ~ 1.5 gCm²day (Fig. 3c,d).

3.1.2 Analysis at national scale

Figures 4a and 4b show the uncertainty reduction for two-week-and country-mean NEE in July and December respectively. The countries and corresponding estimates of prior and posterior uncertainties are listed in Table A2. The results suggest the ability of the mesoscale inversion framework to derive estimates of the NEE at the national scales with relatively low uncertainties. The uncertainty reduction is particularly large for countries such as Germany, France and the UK e.g., more than 80% for France during July. It is larger than 50% for a large majority of the countries in Western Europe and Scandinavia both in July and December.

The smallest uncertainty reduction applies to southeastern European countries where it can be smaller than 10 % (e.g., for Greece in July) indicating that the presence of stations very close to or within a given country is a requisite for bringing significant improvement to the estimates of NEE in this country. In general, the differences of the inversion skill between July and December look consistent with what has been analyzed at the pixel scale. In particular the uncertainty reduction is higher in July for western [European](#) countries but higher in December for eastern [European](#) countries for the same reasons as that given when analyzing the same behavior at the pixel scale (see Sect. 3.1.1).

3.1.3 Analysis at the European scale

Table 1 shows that the uncertainty in two-week-mean NEE in July averaged over the full European domain (6.8×10^6 km² of land surface) is reduced by the inversion by 50% down to a value of ~ 43 TgCmonth⁻¹ (see Table 1 for details) using the default configuration. The

606 uncertainty reduction for December is 66%, resulting in a posterior uncertainty of ~26
607 TgCmonth^{-1} . The uncertainty reduction for the whole European domain is thus higher in
608 December than in July. More precisely, while easterly winds in December strongly favor this
609 period in terms of uncertainty reduction in Eastern Europe, the uncertainty reduction for NEE
610 averaged over the reduced western European domain defined in Fig. 1c does not vary
611 significantly with the season (66% and 64% for July and December respectively). This lack of
612 seasonal variation of the uncertainty reduction at the scale of the western European domain
613 (where most of the ICOS23 stations are located) seems to contrast with the grid-scale and
614 national scale estimations in this domain which indicates that the uncertainty reduction is
615 generally significantly higher during summer than during winter. This contrast will be analyzed
616 and interpreted in Sect. 3.1.4.

Deleted: scales

Deleted: the

618 **3.1.4 Analysis of the variations of the uncertainty as a function of the spatial aggregation of** 619 **the NEE: interpretation of the results obtained at the national and European scales**

620 In order to examine here the dependency of the NEE uncertainty reduction to increasing spatial
621 scales of aggregation for the analyses in July and December, we choose five locations at which
622 we define centered areas with increasing size for which uncertainties in the average NEE are
623 derived. These stations are located using the green circles in Fig. 1c. The five locations
624 correspond to three observing sites of ICOS23: Trainou (TRN), Ochsenkopf (OXK), Plateau
625 Rosa (PRS); one site of ICOS50: SMEAR II-ICOS Hyytiälä (HYY); and one point in Sweden
626 which does not correspond to any site of the ICOS networks tested here, called SW1 hereafter
627 (Fig. 1c). We compute the uncertainty reductions of the two-week mean NEE for July and
628 December over five squares centered around each site and of increasing size (in square degrees):
629 $1.5^\circ \times 1.5^\circ$, $2.5^\circ \times 2.5^\circ$, $3.5^\circ \times 3.5^\circ$, $4.5^\circ \times 4.5^\circ$ and $10.5^\circ \times 10.5^\circ$ respectively (which corresponds to
630 surfaces of different size in terms of km^2). Depending on their location and on their size, the

Deleted: chose

634 corresponding domains expand over areas of Europe that are more or less constrained by the
635 inversion at the pixel scale. But the variations of the uncertainty reduction when increasing the
636 size of these domains are also strongly driven by the spatial correlations in the prior and
637 posterior uncertainty. The results are displayed in Fig. 5.

638 The five locations used for this analysis are representative of the diversity of the situation
639 regarding the differences between grid scale uncertainty reduction in July and in December.

640 While the uncertainty reduction is slightly larger in July than in December for TRN, ~~and~~ much
641 larger in July for PRS and HYY, it is slightly larger in December at OXK and much larger in
642 December at SW1. Furthermore, the values for these grid scale uncertainty reductions range
643 from 15% to 50% in July and from 7% to 47% in December at these locations (Fig. 5).

644 The maximum scores of uncertainty reduction occur for spatial scales of aggregation ranging
645 from 10^5 km^2 to 10^6 km^2 when considering the sites located in Western Europe. These scales
646 approximately correspond to the range of the sizes of the European countries and it is larger than
647 the typical area of correlation of the prior uncertainty (as defined by prior correlation lengths of
648 250 km). Increasing the spatial resolution generally increases the uncertainty reduction since
649 posterior uncertainties have generally smaller correlation lengths than prior uncertainties, due to
650 the spatial attribution error when trying to link the measurement information to local fluxes
651 despite the atmospheric mixing. This explains the increase of uncertainty reduction from the grid
652 scale to the “national scales”. This also explains why, for a given regional density of the
653 measurement network, larger countries bear larger uncertainty reductions (Fig. 4). However,
654 above such national scales, the corresponding domains include parts of Eastern Europe being
655 poorly sampled by the ICOS23 network which explains the decrease in uncertainty reduction.

656 The convergence between the results around TRN, PRS and OXK in December and July (which
657 tend to nearly 65% uncertainty reduction when the averaging area reaches the western European
658 domain), between the results around all sites in December (which tend to 66% uncertainty

Deleted: ,

reduction when the averaging area reaches the whole of Europe), or between the results around all sites in July (which tend to nearly 53% uncertainty reduction when the averaging area reaches the whole of Europe), starts between the 10^5km^2 and 10^6km^2 (national scale) averaging areas. For smaller areas, the differences between results in July and December or between results for different spatial locations stay similar to what is seen at the $0.5^\circ \times 0.5^\circ$ scale.

The similarity of the results for the western European domain despite differences at the grid scale in July and December can be explained by differences of correlations between areas at scales similar or larger than the national scale in the posterior uncertainties (since the correlations of the prior uncertainties aggregated at the national scale or at larger scales are very close for July and December). Figure 6 illustrates the variations of such correlations of the posterior uncertainty at the national scale between July and December using the example of correlations between Germany and other countries. These correlations are usually more negative in December, which indicates a larger difficulty in December than in July to distinguish in the information from the measurement network the separate contributions of the different neighboring countries (or of different areas of larger size). This can be attributed to the stronger winds in December which increase the extent of the flux footprints of the concentration measurements. Such an increase of the footprints in December limit the ability to solve for the fluxes in the vicinity of the measurement sites but increase the ability to solve for the fluxes at large scales.

678

3.2 Impact of the extension of the ICOS network

The effect on local (grid scale) uncertainty reduction of assimilating data from new sites in the ICOS network depends on the coverage of the area by the initial ICOS23 network, as illustrated by the comparison of the results using ICOS23, ICOS50 and ICOS66 and the reference configuration of the inversion (see Figs. 2 and 7). For example, adding one new site in Sweden or Finland yields a stronger increase of the uncertainty reduction than adding one site in the

central part of Western Europe, where the network is already rather dense. Since most of the new sites from ICOS23 to ICOS50 and then ICOS66 are located in Western Europe, the improvements due to adding 27 or 43 sites to ICOS23 do not thus appear to be as critical as what can be achieved using the 23 sites of ICOS23. The changes from ICOS23 to ICOS50 significantly enhance the uncertainty reduction at 0.5° resolution in Western Europe in July, e.g., with uncertainty reduction increased from ~40% using ICOS23 to ~60% using ICOS66 in Switzerland. The impact of adding new sites is larger in December than in July, and, consequently, results for western Germany and Benelux converge between July and December when increasing the network to ICOS66.

The impact on the scores of uncertainty reduction of the increase of the ICOS network is also significant at the national (compare Fig. 4 and Fig. 8) and European scales (see Table 1 and Fig. 9) when comparing results with ICOS50 or ICOS66 to those obtained with ICOS23. The ICOS66 network delivers uncertainty reductions as high as 80% for countries like France and Germany in July. For Europe, the uncertainty reduction when using ICOS66 reaches 79% down to ~15 TgCmonth⁻¹ posterior uncertainty in December, and 64% down to ~33 TgCmonth⁻¹ posterior uncertainty in July. However, the increase from ICOS50 to ICOS66 does not seem to impact much the uncertainty reduction at these scales, especially in July.

Figure 9 illustrates the diversity (depending on the space locations) of the evolution of the impact of increasing the network as a function of the NEE averaging spatial scale. For a low altitude site already present in the dense part of ICOS23, the impact of adding new sites increases when increasing the spatial scale of the analysis up to areas where ICOS23 is less dense (mainly in Eastern Europe) and where new sites are included in ICOS50. Conversely, the impact of the addition of new sites can decrease when increasing the NEE spatial aggregation scale, e.g., at HYY where a new site is specifically added in ICOS50.

Deleted: even

Deleted: The impact also increases for SW1 (which is located in the northeastern border of the domain) with increasing spatial aggregation scale since encompassing more and more of the new sites from ICOS23 to ICOS50 when extending the averaging domain to the European western area.

3.3 Sensitivity to the correlation length of the prior uncertainty

The impact of reducing the correlation e-folding length (from 250 km to 150 km) of the prior uncertainty in the inversion configuration is tested using ICOS66 in July (compare Figs. 7b and 10a, Figs. 8b and 11a, and the corresponding curves in Fig. 9). Such a change of correlation length strongly decreases the values of uncertainty reduction at all spatial scales. This is because it decreases the prior uncertainty at every scale while decreasing the ability of the inversion system to extrapolate in space the information from measurement sites based on the knowledge about spatial correlations of the prior uncertainties. At 0.5° resolution, the areas of high uncertainty reduction narrow around the measurement sites and the smaller overlap of the areas of influence of these sites limits the highest local values of uncertainty reduction to 40%-50% while typical values in Western Europe now range from 20% to 40% instead of 30% to 65% when using \mathbf{B}_{250} (see Sect. 2.2.2 for the definition of the \mathbf{B} matrices). The uncertainty reduction for countries such as the UK, Germany and Spain decreases when the e-folding correlation length is lowered from 250 km to 150 km, from more than 75%-80% to less than 70%. For the full European domain, it decreases from 64% to 47%.

Even though these reductions can be very large, it is important to keep in mind that they refer to uncertainty reductions compared to a prior uncertainty which is decreased by the new configuration of \mathbf{B} (as illustrated at the country scale in Fig. A1). The posterior uncertainty in the European and two-week mean NEE in July using ICOS66 is decreased from $\sim 33 \text{ TgC month}^{-1}$ to $29 \text{ TgC month}^{-1}$ when changing the configuration of \mathbf{B} from \mathbf{B}_{250} to \mathbf{B}_{150} (Table 1). Similarly, the posterior uncertainty is generally smaller at the national scale when changing the configuration of \mathbf{B} from \mathbf{B}_{250} to \mathbf{B}_{150} (Fig. A2). We thus have an expected situation for which improving the knowledge on the prior NEE improves that of the posterior NEE even if in our case, the improvement of the knowledge on the prior NEE which is tested here also decreases the ability to extrapolate in space the information from the atmospheric measurements. However, of note is

Deleted: decreases

Deleted: critical

that when changing the configuration of \mathbf{B} from \mathbf{B}_{250} to \mathbf{B}_{150} , i.e., when changing the spatial correlations between prior uncertainties at 0.5° resolution, but not the standard deviations of the prior uncertainties at 0.5° resolution, we do not improve the knowledge on the prior NEE at the model grid 0.5° resolution. Given the lower uncertainty reduction when using \mathbf{B}_{150} , the posterior uncertainties are higher at 0.5° resolution when changing the configuration of \mathbf{B} from \mathbf{B}_{250} to \mathbf{B}_{150} (Fig. A3).

3.4 Sensitivity to the observation error

The impact of dividing the standard deviation of the observation error by two in the inversion configuration is tested using ICOS50 in July (compare Figs. 7a and 10b, Figs. 8a and 11b and the corresponding curves in Fig. 9). The decrease of observation error increases the weight of the measurements in the inversion and the resulting uncertainty reduction. This increase is visible at all spatial scales for the aggregation of the NEE, and relatively constant as a function of these spatial scales except at the European scale (for which the uncertainty reduction is equal to 67% when dividing the observation error by two instead of 64% when using the default configuration of this error). This provides the highest scores of uncertainty reduction of this study at any spatial scales, the impact of division of the observation error by two being larger than that of increasing the ICOS network configuration from ICOS50 to ICOS66.

Deleted: for which it is smaller, from 64% to 67%.

4 Synthesis and conclusions

We assessed the potential of CO_2 mole fraction measurements from three configurations of the ICOS atmospheric network to reduce uncertainties in two-week mean European NEE at various spatial scales in northern summer and in northern winter. This assessment is based on a regional variational inverse modeling system with parameters consistent with the knowledge on

772 uncertainties in prior estimates of NEE from ecosystem models and in atmospheric transport
773 models. The results obtained with the various experiments from this study indicate an
774 uncertainty reduction which ranges between ~50% and 80% for the full European domain,
775 between ~70% and 90% for large countries in Western Europe (such as France, Germany, Spain,
776 UK), where the ICOS network is denser, but below 50% in much cases for eastern countries
777 where there are few ICOS sites even with the ICOS66 configuration. At 0.5° resolution,
778 excluding results when using B_{150} (for which the uncertainty reduction is applied to a different
779 prior uncertainty), uncertainty reductions range from 30% to 65% in the dense parts of the
780 networks (between northern Spain and eastern Germany) while it is generally below 30% east of
781 Germany and Italy when using ICOS23 or east of Poland and Hungary when using ICOS66. The
782 very high values of uncertainty reduction obtained in areas where ICOS sites are distant by less
783 than the typical length scale of the prior uncertainty (Western Europe when using ICOS23 and a
784 larger area when using ICOS66) is highly promising for provision of accurate monitoring of the
785 NEE in these areas in the near term.

Deleted: the precision

Deleted: the

786 Despite the absence of seasonal variation for the uncertainty in the average NEE over Western
787 Europe (at least according to our results for the year 2007) significant seasonal variations at
788 higher resolution or for the full European domain reveal the influence of the atmospheric
789 transport on the scores of uncertainty reduction. Using ICOS66 instead of ICOS23 does not limit
790 this behavior since few sites are added between ICOS23 and ICOS66 in Eastern Europe where
791 the largest seasonal variations of the uncertainty reduction occur. The larger wind speed in
792 December than in July explains that there is a similar uncertainty reduction in July and
793 December for Western Europe. This is another illustration of the influence of the atmospheric
794 transport on the scores of uncertainty reduction. It demonstrates that such scores and their
795 sensitivity to the network extension can hardly be anticipated based on a simple analysis of the
796 site locations and on the knowledge of the typical spatial scale of a station footprint. Their
797 derivation requires the complex application of an inversion system as in this study.

Deleted: such

801 These scores of uncertainty reduction result in posterior uncertainties lower than $1.8 \text{ gC m}^{-2} \text{ day}^{-1}$
 802 at 0.5° resolution in the areas where the ICOS network is dense. At the national scale, posterior
 803 uncertainties scales are compared to the typical estimates of the NEE from the ORCHIDEE
 804 model for the corresponding two-week period in July 2007 in Table A2. The relative posterior
 805 uncertainty could be less than 20% for the countries having the largest NEE such as France,
 806 Germany, Poland or UK (if using ICOS66 in the three last cases, otherwise it should be less than
 807 30% if using ICOS23), even though it would not be the case for Scandinavian countries with a
 808 high NEE. For some Eastern European countries, the posterior uncertainty could be very close to
 809 the estimate of NEE from ORCHIDEE but the general tendency is to obtain posterior
 810 uncertainties much lower than the estimate of the NEE from ORCHIDEE even when using
 811 ICOS23. This tendency is reflected at the European scale (Table 1) for which the posterior
 812 uncertainty when using ICOS23 and the reference inversion configuration is $\sim 20\%$ and $\sim 30\%$ of
 813 the total NEE from ORCHIDEE in July and December, respectively. These numbers can be
 814 compared to the uncertainty targets defined for the CarbonSat satellite mission (ESA, 2015; of
 815 note is that the mission has not been selected for the Earth Explorer 8 opportunity): 0.5 gC m^{-2}
 816 day^{-1} at the $500 \text{ km} \times 500 \text{ km}$ and 1 month scale. Figures 12, A1 and A2 show that at the 2-week
 817 and national scale, the prior uncertainties are systematically larger than this target, but that the
 818 posterior uncertainties in Western and Northern Europe are generally close or smaller than this
 819 target even when using ICOS23. Since the temporal correlations in the prior uncertainty have a 1
 820 month timescale and since the temporal correlations in the posterior uncertainty should be
 821 smaller than those in the prior uncertainty, these uncertainties at the 2-week scale can be
 822 considered to be equal or lower than the corresponding uncertainties at the 1 month scale.
 823 Therefore, Figures 12, A1 and A2 indicate that the inversion is required to reach the target of 0.5
 824 $\text{gC m}^{-2} \text{ day}^{-1}$ at the $500 \text{ km} \times 500 \text{ km}$ and 1 month scale. They also indicate that this target is
 825 likely not reached in a large part of South Eastern Europe even when using ICOS66 but that for
 826 countries like the Czech Republic and Poland, extending the network from ICOS23 to ICOS66

Deleted: that

Deleted: from the CarbonSat report for mission selection.

830 | allows to reach it. Finally, these figures indicate that the ICOS23 network is sufficient to reach
831 | this target in Western Europe.

Deleted: reaching

832 | The comparison of the sensitivity of the results in July to changes in the observation network,
833 | correlation lengths of the prior uncertainty and observation error (in the range of tests conducted
834 | in this study) indicates a hierarchy of the impact of such changes which depends on the spatial
835 | scales. Increasing the network from ICOS23 to ICOS50 yields the largest change in posterior
836 | uncertainty due to a significantly better monitoring of the eastern part of Europe. However, for
837 | western European countries, at the grid to national scales, the impact of changing the inversion
838 | parameters is generally larger than that of the increase of the network size. Given the range of
839 | spatial correlations in the prior uncertainty that are investigated here, the spacing of ICOS sites
840 | in Western Europe is already sufficiently narrow to ensure that this full domain is significantly
841 | constrained by the measurements from ICOS23. The weight of this constraint at grid to national
842 | scales in Western Europe is more directly modified by dividing by two the observation errors or
843 | shortening by nearly half the correlation length of the prior uncertainties than by doubling the
844 | number of monitoring sites.

Deleted: depending

845 | The increase of the ICOS network from ICOS23 to ICOS50 or to ICOS66 follow two strategies:
846 | a densification of the European network in the West and its extension in the poorly monitored
847 | area, mainly in the East. The results of this study indicate that the extension should presently
848 | focus in the East since notional targets for the posterior uncertainty in national scale NEE
849 | (derived from the CarbonSat report for mission selection) are reached in Western Europe when
850 | using ICOS23, since the posterior uncertainties from the national scale to the 0.5° scale in
851 | Western Europe are weakly sensitive to the increase of the network, and since the results in
852 | Eastern Europe are highly sensitive to the increase in the size of the network.. These results also
853 | raise optimism regarding the increase of the accuracy in the inverted NEE from improvements of
854 | the atmospheric transport modeling or from the improvement of the prior “bottom-up” (as

Deleted: it

Deleted: precision

859 opposed to the “top-down” information from atmospheric concentrations) knowledge on the
860 fluxes.

861 Some limitations of the calculations in this paper should be kept in mind when analyzing the
862 results more precisely. The convergence of the calculations as a function of the number of
863 minimization iterations during the inversion or as a function of the number of inversions in each
864 Monte Carlo ensemble experiment, has been assessed based on average diagnostics. Locally,
865 some results have not converged. Additionally, the use of ICOS50 or ICOS66 should require
866 more minimization iterations to converge to the same extent as when using ICOS23 or ICOS50
867 due to the increase of the dimension of the inversion problem. As an example, this results in very
868 slight increases of the posterior uncertainty for Sweden or for Europe when extending ICOS50 to
869 ICOS66. This problem of convergence slightly **changes** the scores of uncertainty reduction **only**
870 for specific areas, but it is not significant enough to impact the typical range of values analyzed
871 and the subsequent conclusions in this study.

Deleted: the diagnostic of

Deleted: (which do not yield significant relative differences)

Deleted: alter

Deleted: only

872 Another point to note is that the confidence in the reference configuration of the inversion has
873 been built based on the diagnostics of the errors in NEE simulated with the ORCHIDEE model
874 at the local scale from Chevallier et al. (2012) and at the monthly and Europe wide scale from
875 Broquet et al. (2013). A simple model is used to represent the correlations of the prior
876 uncertainty in NEE and thus the prior uncertainty in NEE at the intermediate scales. The
877 modeling of the prior uncertainties may need to be refined to better account for the heterogeneity
878 of the European ecosystems with potential impact on the results of posterior uncertainty at fine
879 scales. Furthermore, the assumption that the uncertainties in CO₂ anthropogenic emissions do not
880 have a significant signature at the ICOS sites is based on studies at relatively few monitoring
881 sites corresponding to the coarse atmospheric network of the CarbonEurope-IP project (Schulze
882 et al. 2010). When considering far denser networks with many sites close to urban areas (such as
883 in and around the Netherlands when using ICOS66), this uncertainty should be accounted for.

889 The assumption that uncertainties in the boundary conditions and in the anthropogenic emissions
890 have a weak impact on the inversion is also supported by the results of Broquet et al. (2013) but
891 only at the European scale. ~~However,~~ when assessing results for specific areas in highly
892 industrialized countries or close to the model domain boundaries such as in this study, the impact
893 of such uncertainties may be larger ~~than~~ when analyzing results at the European scale. Such
894 considerations should lead to further investigation regarding the inversion configuration and thus
895 potential refinement of the results.

Deleted: only. But

Deleted:

896 This study focuses on results for two-week mean fluxes while a critical target of the inversion
897 should be related to annual mean fluxes. This and the strong influence of the variations of the
898 meteorological conditions on the inversion results (which limits the ability to extrapolate the
899 results to the annual scale) encourage the set-up of 1-year long experiments. However, this study
900 already gives qualitative insights on such results and on their sensitivity to the observing network
901 or to accuracy of the different components of the system which should support future network
902 design studies in Europe. By demonstrating the capability for deriving scores of uncertainty
903 reductions for NEE at 6-hour and 0.5° resolution, it supports the development of operational
904 inversion systems deriving the optimal location for new sites to be installed in the European
905 network.

906

907

908

909

910

911

914 **Acknowledgement**

915 This study was co-funded by the European Commission under the EU Seventh Research
916 Framework Programme (grant agreement No. 283080, Geocarbon project) and under the
917 framework of the preparatory phase of ICOS. It was also co-funded by the industrial chair
918 BridGES (supported by the Université de Versailles Saint-Quentin-en-Yvelines, the
919 Commissariat à l’Energie Atomique et aux Energies Renouvelables, the Centre National de la
920 Recherche Scientifique, Thales Alenia Space and Veolia). We also would like to thank the
921 partners of the ICOS infrastructure for providing a list of potential locations for future ICOS
922 atmospheric sites.

923

924

925

926

927

928

929

930

931

932

933

934

935

936

937

938

939

940

References

- Ahmadov, R., Gerbig, C., Kretschmer, R., Körner, S., Rödenbeck, C., Bousquet, P., and Ramonet, M.: Comparing high resolution WRF-VPRM simulations and two global CO₂ transport models with coastal tower measurements of CO₂, *Biogeosciences*, 6, 807-817, doi:10.5194/bg-6-807-2009, 2009.
- Bocquet, M.: Grid resolution dependence in the reconstruction of an atmospheric tracer source, *Nonlin. Processes Geophys.*, 12, 219–234, 2005.
- Bousserez, N., Henze, D. K., Perkins, A., Bowman, K. W., Lee, M., Liu, J., Deng, F., and Jones, D. B. A.: Improved analysis-error covariance matrix for high-dimensional variational inversions: application to source estimation using a 3-D atmospheric transport model, *Q. J. Roy. Meteor. Soc.*, doi:10.1002/qj.2495, 19021, 19023, 2015.
- Bréon, F. M., Broquet, G., Puygrenier, V., Chevallier, F., Xueref-Rémy, I., Ramonet, M., Dieudonné, E., Lopez, M., Schmidt, M., Perrussel, O., and Ciais, P.: An attempt at estimating Paris area CO₂ emissions from atmospheric concentration measurements, *Atmos. Chem. Phys.* 15, 1707-1724, doi:10.5194/acp-15-1707-2015, 2015.
- Broquet, G., Chevallier, F., Rayner, P. J., Aulagnier, C., Pison, I., Ramonet, M., Schmidt, M., Vermeulen, A. T., and Ciais, P.: A European summertime CO₂ biogenic flux inversion at mesoscale from continuous in situ mixing ratio measurements, *J. Geophys. Res.*, 116, D23303, doi:10.1029/2011JD016202, 2011
- Broquet, G., Chevallier, F., Bréon, F.-M., Kadygrov, N., Alemanno, M., Apadula, F., Hammer, S., Haszpra, L., Meinhardt, F., Morguí, J. A., Necki, J., Piacentino, S., Ramonet, M., Schmidt, M., Thompson, R. L., Vermeulen, A. T., Yver, C., and Ciais, P.: Regional inversion of CO₂ ecosystem fluxes from atmospheric measurements: reliability of the uncertainty estimates, *Atmos. Chem. Phys.*, 13, 9039-9056, doi:10.5194/acp-13-9039-2013, 2013.
- Chevallier, F., Bréon, F. M., and Rayner, P. J.: Contribution of the Orbiting Carbon Observatory to the estimation of CO₂ sources and sinks: Theoretical study in a variational data assimilation framework, *J. Geophys. Res.*, 112, D09307, doi:10.1029/2006JD007375, 2007.
- Chevallier, F., Wang, T., Ciais, P., Maignan, F., Bocquet, M., Arain A., Cescatti, A., Chen, J., Dolman, A. J., Law, B. E., Margo-lis, H., Montagnani, L., and Moors, E.: What eddy-covariance measurements tell us about prior land flux errors in CO₂-flux inversion schemes, *Global Biogeochem. Cycles*, 26, GB1021, doi:10.1029/2010GB003974, 2012.
- Ciais, P., Dolman, A. J., Bombelli, A., Duren, R., Peregon, A., Rayner, P. J., Miller, C., Gobron, N., Kinderman, G., Marland, G., Gruber, N., Chevallier, F., Andres, R. J., Balsamo, G., Bopp, L., Bréon, F.-M., Broquet, G., Dargaville, R., Battin, T. J., Borges, A., Bovensmann, H., Buchwitz, M., Butler, J., Canadell, J. G., Cook, R. B., DeFries, R., Engelen, R., Gurney, K. R., Heinze, C., Heimann, M., Held, A., Henry, M., Law, B., Luyssaert, S., Miller, J., Moriyama, T., Moulin, C., Myneni, R. B., Nussli, C., Obersteiner, M., Ojima, D., Pan, Y., Paris, J.-D., Piao, S. L., Poulter, B., Plummer, S., Quegan, S., Raymond, P., Reichstein, M., Rivier, L., Sabine, C., Schimel, D., Tarasova, O., Valentini, R., Wang, R., van der Werf, G., Wickland, D., Williams, M., and Zehner, C.: Current systematic carbon-cycle observations and the need for

implementing a policy-relevant carbon observing system, *Biogeosciences*, 11, 3547-3602,
doi:10.5194/bg-11-3547-2014, 2014.

Claeyman, M., Attié, J.-L., Peuch, V.-H., El Amraoui, L., Lahoz, W. A., Josse, B., Joly, M.,
Barré, J., Ricaud, P., Massart, S., Piacentini, A., von Clarmann, T., Höpfner, M., Orphal, J.,
Flaud, J.-M. and Edwards, D. P.: A thermal infrared instrument onboard a geostationary platform
for CO and O₃ measurements in the lowermost troposphere: Observing System Simulation
Experiments (OSSE), *Atmos. Meas. Tech.*, 4, 1637-1661, doi:10.5194/amt-4-1637-2011, 2011.

Edwards, D. P., Arellano Jr., A. F. and Deeter M. N.: A satellite observation system simulation
experiment for carbon monoxide in the lowermost troposphere, *J. Geophys. Res.*, 114, D14304,
doi:10.1029/2008JD011375, 2009.

Enting, I. G.: *Inverse Problems in Atmospheric Constituent Transport*, Cambridge Univ. Press,
Cambridge, U. K., 2002.

Errico, R. M., Yang, R., Privé, N. C., Tai, K.-S., Todling, R., Sienkiewicz, M. E. and Guo, J.:
Development and validation of observing-system simulation experiments at NASA's Global
Modeling and Assimilation Office. *Q.J.R. Meteorol. Soc.*, 139: 1162–1178, doi: 10.1002/qj.2027,
2013.

ESA, Report for Mission Selection: CarbonSat, ESA SP-1330/1, (2 volume series), European
Space Agency, Noordwijk, The Netherlands, 2015.

Francey, R.J. (Ed.): Report of the Ninth WMO meeting of experts on carbon dioxide
concentration and related tracer measurement techniques. Aspendale, Vic., Australia, 1–4
September 1997, World Meteorological Organization (WMO), Geneva, Series: Global
Atmosphere Watch (GAW); no. 132; WMO; TD no. 952, 132 pp., 1998.

Gerbig, C., Lin, J. C., Munger, J. W., and Wofsy, S. C.: What can tracer observations in the
continental boundary layer tell us about surface-atmosphere fluxes?, *Atmos. Chem. Phys.*, 6,
539-554, doi:10.5194/acp-6-539-2006, 2006.

Gilbert, J. C., and Lemaréchal, C.: Some numerical experiments with variable-storage quasi-
Newton algorithms, *Math. Program.*, 45, 407–435, 1989.

Göckede, M., Turner, D. P., Michalak, A. M., Vickers, D. and Law B. E.: Sensitivity of a
subregional scale atmospheric inverse CO₂ modeling framework to boundary conditions, *J.*
Geophys. Res., 115, D24112, doi:10.1029/2010JD014443, 2010.

Gurney, K. R., Law, R. M., Denning, A. S., Rayner, P. J., Baker, D., Bousquet, P., Bruhwiler, L.,
Chen, Y.-H., Ciais, P., Fan, S., Fung, I. Y., Gloor, M., Heimann, M., Higuchi, K., John, J., Maki,
T., Maksyutov, S., Masarie, K., Peylin, P., Prather, M., Pak, B. C., Randerson, J., Sarmiento, J.,
Taguchi, S., Takahashi, T., and Yuen, C.-W.: Towards robust regional estimates of CO₂ sources
and sinks using atmospheric transport models, *Nature*, 415, 626–630, 2002.

Halliwell Jr., G. R., Srinivasan, A., Kourafalou, V., Yang, H., Willey, D., Le Hénaff, M. and
 Atlas, R.: Rigorous Evaluation of a Fraternal Twin Ocean OSSE System for the Open Gulf of
 Mexico. *J. Atmos. Oceanic Technol.*, **31**, 105–130, doi: 10.1175/JTECH-D-13-00011.1, 2014.
 Hourdin, F., Musat I., Bony S., Braconnot P., Codron F., Dufresne J. L., Fairhead L., Filiberti M.
 A., Friedlingstein P., Grandpeix J. Y., Krinner G., LeVan P., Li Z.X., Lott F.: The LMDZ4
 general circulation model: Climate performance and sensitivity to parametrized physics with
 emphasis on tropical convection, *J. Clim. Dyn.*, **27**, 787–813, doi:10.1007/s00382-006-0158-0,
 2006.
 Houweling, S., Breon, F.-M., Aben, I., Rödenbeck, C., Gloor, M., Heimann, M., and Ciais, P.:
 Inverse modeling of CO₂ sources and sinks using satellite data: a synthetic inter-comparison of
 measurement techniques and their performance as a function of space and time, *Atmos. Chem.*
Phys., **4**, 523–538, doi:10.5194/acp-4-523-2004, 2004.
 Hungershofer, K., Breon, F.-M., Peylin, P., Chevallier, F., Rayner, P., Klonecki, A.,
 Houweling, S., and Marshall, J.: Evaluation of various observing systems for the global
 monitoring of CO₂ surface fluxes, *Atmos. Chem. Phys.*, **10**, 10503–10520, doi:10.5194/acp-10-
 10503-2010, 2010.
 Kadyrov, N., Maksyutov, S., Eguchi, N., Aoki, T., Nakazawa, T., Yokota, T., and Inoue, G.:
 Role of simulated GOSAT total column CO₂ observations in surface CO₂ flux uncertainty
 reduction, *J. Geophys. Res.*, **114**, D21208, doi:10.1029/2008JD011597, 2009.
 Krinner, G., Viovy, N., de Noblet-Ducoudré, N., Ogée, J., Polcher, J., Friedlingstein, P., Ciais,
 P., Sitch, S., and Prentice, I. C.: A dynamic global vegetation model for studies of the coupled
 atmosphere-biosphere system, *Global Biogeochem. Cycles*, **19**, GB1015, doi:10.1029/
 2003GB002199, 2005.
 Lauvaux, T., Uliasz, M., Sarrat, C., Chevallier, F., Bousquet, P., Lac, C., Davis, K. J., Ciais, P.,
 Denning, A. S., and Rayner, P. J.: Mesoscale inversion: first results from the CERES campaign
 with synthetic data, *Atmos. Chem. Phys.*, **8**, 3459–3471, doi:10.5194/acp-8-3459-2008, 2008.
 Lauvaux, T., Schuh, A. E., Uliasz, M., Richardson, S., Miles, N., Andrews, A. E., Sweeney, C.,
 Diaz, L. I., Martins, D., Shepson, P. B., and Davis, K. J.: Constraining the CO₂ budget of the
 corn belt: exploring uncertainties from the assumptions in a mesoscale inverse system, *Atmos.*
Chem. Phys., **12**, 337–354, doi:10.5194/acp-12-337-2012, 2012.
 Law, R. M., Peters, W., Roedenbeck, C., Aulagnier, C., Baker, I., Bergmann, D. J., Bousquet, P.,
 Brandt, J., Bruhwiler, L., Cameron-Smith, P. J., Christensen, J. H., Delage, F., Denning, A. S.,
 Fan, S., Geels, C., Houweling, S., Imasu, R., Karstens, U., Kawa, S. R., Kleist, J., Krol, M. C.,
 Lin, S. J., Lokupitiya, R., Maki, T., Maksyutov, S., Niwa, Y., Onishi, R., Parazoo, N., Patra, P.
 K., Pieterse, G., Rivier, L., Satoh, M., Serrar, S., Taguchi, S., Takigawa, M., Vautard, R., Ver-
 meulen, A. T., and Zhu, Z.: TransCom model simulations of hourly atmospheric CO₂:
 Experimental overview and diurnal cycle results for 2002, *Global Biogeochem. Cycles.*, **22**,
 GB3009, doi:10.1029/2007gb003050, 2008.
 Marécal, V., Peuch, V.-H., Andersson, C., Andersson, S., Arteta, J., Beekmann, M., Benedictow,
 A., Bergström, R., Bessagnet, B., Cansado, A., Chéroux, F., Colette, A., Coman, A., Curier, R.
 L., Denier van der Gon, H. A. C., Drouin, A., Elbern, H., Emili, E., Engelen, R. J., Eskes, H. J.,
 Foret, G., Friese, E., Gauss, M., Giannaros, C., Guth, J., Joly, M., Jaumouillé, E., Josse, B.,
 Kadyrov, N., Kaiser, J. W., Krajsek, K., Kuenen, J., Kumar, U., Liora, N., Lopez, E., Malherbe,

1086 L., Martinez, I., Melas, D., Meleux, F., Menut, L., Moinat, P., Morales, T., Parmentier, J.,
 1087 Piacentini, A., Plu, M., Poupkou, A., Queguiner, S., Robertson, L., Rouil, L., Schaap, M., Segers,
 1088 A., Sofiev, M., Tarasson, L., Thomas, M., Timmermans, R., Valdebenito, Á., van Velthoven, P.,
 1089 van Versendaal, R., Vira, J., and Ung, A.: A regional air quality forecasting system over Europe:
 1090 the MACC-II daily ensemble production, *Geosci. Model Dev.*, 8, 2777-2813, doi:10.5194/gmd-
 1091 8-2777-2015, 2015.
 1092
 1093 Masutani, M., Schlatter, T. W., Errico, R. M., Stoffelen, A., Andersson, E., Lahoz, W., Woollen,
 1094 J. S., Emmitt, G. D., Riishøjgaard, L.-P. and Lord, S. J.: "Observing System Simulation
 1095 Experiments" in *Data Assimilation: Making sense of observations*, Eds. Lahoz, W. A., Khattatov
 1096 B. and Ménard, R., Springer, Berlin, pp 647-679, 2010.
 1097
 1098 Meesters, A. G. C. A., Tolk, L.F., Peters, W., Hutjes, R. W. A., Velinga, O.S., Elbers, J.A.,
 1099 Vermeulen, A.T., van der Laan, S., Neubert, R. E. M., Meijer, H. A. J. and Dolman, A. J.: Inverse
 1100 carbon dioxide flux estimates for the Netherlands, *J. Geophys. Res.*, 117, D20306,
 1101 doi:10.1029/2012JD017797, 2012.
 1102
 1103 Peters, W., Krol, M. C., Van Der Werf, G. R., Houweling, S., Jones, C. D., Hughes, J., Schaefer,
 1104 K., Masarie, K. A., Jacobson, A. R., Miller, J. B., Cho, C. H., Ramonet, M., Schmidt, M.,
 1105 Ciattaglia, L., Apadula, F., Heltai, D., Meinhardt, F., Di Sarra, A. G., Piacentino, S., Sferlazzo,
 1106 D., Aalto, T., Hatakka, J., Strom, J., Haszpra, L., Meijer, H. A. J., Van Der Laanm, S., Neubert,
 1107 R. E. M., Jordan, A., Rodo, X., Morgui, J.-A., Vermeulen, A. T., Popa, E., Rozanski, K.,
 1108 Zimnoch, M., Manning, A. C., Leuenberger, M., Uglietti, C., Dolman, A. J., Ciais, P., Heimann,
 1109 M. and Tans, P. P.: Seven years of recent European net terrestrial carbon dioxide exchange
 1110 constrained by atmospheric observations. *Global Change Biology*, 16: 1317–1337.
 1111 doi: 10.1111/j.1365-2486.2009.02078.x, 2010.
 1112
 1113 Peylin, P., Houweling, S., Krol, M. C., Karstens, U., Rödenbeck, C., Geels, C., Vermeulen, A.,
 1114 Badawy, B., Aulagnier, C., Pregar, T., Delage, F., Pieterse, G., Ciais, P., and Heimann, M.:
 1115 Importance of fossil fuel emission uncertainties over Europe for CO₂ modeling: model
 1116 intercomparison, *Atmos. Chem. Phys.*, 11, 6607-6622, doi:10.5194/acp-11-6607-2011, 2011.
 1117
 1118 Peylin, P., Law, R. M., Gurney, K. R., Chevallier, F., Jacobson, A. R., Maki, T., Niwa, Y.,
 1119 Patra, P. K., Peters, W., Rayner, P. J., Roedenbeck, C., van der Laan-Luijkx, I. T., and Zhang, X.:
 1120 Global atmospheric carbon budget: results from an ensemble of atmospheric CO₂ inversions,
 1121 *Biogeosciences*, 10, 6699-6720, doi:10.5194/bg-10-6699-2013, 2013.
 1122
 1123 Rayner, P. J., Enting, I.G., and Trudinger, C. M.: Optimizing the CO₂ observing network for
 1124 constraining sources and sinks, *Tellus B*, 48(4), 433-444, 1996.
 1125
 1126 Riishøjgaard, L. P., Ma, Z., Masutani, M., Woollen, J. S., Emmitt, G. D., Wood, S. A.
 1127 and Greco, S.: Observation system simulation experiments for a global wind observing
 1128 sounder, *Geophys. Res. Lett.*, 39, L17805, doi:10.1029/2012GL051814, 2012.
 1129
 1130 Roedenbeck, C., Houweling, S., Gloor, M., and Heimann, M.: CO₂ flux history 1982–2001
 1131 inferred from atmospheric data using a global inversion of atmospheric transport, *Atmos. Chem.*
 1132 *Phys.*, 3, 1919-1964, doi:10.5194/acp-3-1919-2003, 2003.
 1133
 1134 Schmidt, H., Derognat, C., Vautard, R., and Beekmann, M.: A comparison of simulated and
 1135 observed ozone mixing ratios for the summer of 1998 in Western Europe, *Atmos. Environ.*,
 1136 35(36), 6277–6297, doi:10.1016/S1352-2310(01)00451-4, 2001.
 1137

1138 Schuh, A. E., Denning, A. S., Corbin, K. D., Baker, I. T., Uliasz, M., Parazoo, N., Andrews, A.
 1139 E., and Worthy, D. E. J.: A regional high-resolution carbon flux inversion of North America for
 1140 2004. *Biogeosciences* 7, 1625–1644, doi: 10.5194/bg-7-1625-2010, 2010.
 1141
 1142 Schulze, E. D., Ciais, P., Luyssaert, S., Schrumpf, M., Janssens, I. A., Thiruchittampalam, B.,
 1143 Theloke, J., Saurat, M., Bringezu, S., Lelieveld, J., Lohila, A., Rebmann, C., Jung, M.,
 1144 Bastviken, D., Abril, G., Grassi, G., Leip, A., Freibauer, A., Kutsch, W., Don, A., Nieschulze, J.,
 1145 Borner, A., Gash, J. H., and Dolman, A. J.: The European carbon balance. Part 4: integration of
 1146 carbon and other trace-gases fluxes, *Global Change Biol.*, 16, 1451–1469, 2010.
 1147
 1148 Takahashi, T., Sutherland, S. C., Wanninkhof, R., Sweeney, C., Feely, R. A., Chipman, D. W.,
 1149 Hales, B., Friederich, G., Chavez, F., Sabine, C., Watson, A., Bakker, D. C. E., Schuster, U.,
 1150 Metzl, N., Yoshikawa-Inoue, H., Ishii, M., Midorikawa, T., Nojiri, Y., Körtzinger, A.,
 1151 Steinhoff, T., Hoppema, M., Olafsson, J., Arnarson, T. S., Tilbrook, B., Johannessen, T.,
 1152 Olsen, A., Bellerby, R., Wong, C. S., Delille, B., Bates, N. R., and de Baar, H. J. W.:
 1153 Climatological mean and decadal change in surface ocean pCO₂, and net sea-air CO₂ flux over
 1154 the global oceans, *Deep-Sea Research II* 56(8-10), pp. 554-577 .doi:10.1016/j.dsr2.2008.12.009,
 1155 2009.
 1156
 1157 Timmermans, R. M. A., Schaap, M., Elbern, H., Siddans, R., Tjemkes, S., Vautard, R. and
 1158 Builtjes, P.: An Observing System Simulation Experiment (OSSE) for Aerosol Optical Depth
 1159 from Satellites. *J. Atmos. Ocean Tech.*, **26**, 2673-2682, 2009a.
 1160
 1161 Timmermans, R. M. A., Segers, A. J., Builtjes, P. J. H., Vautard, R., Siddans, R., Elbern, H.,
 1162 Tjemkes, S. A. T. and Schaap, M.: The added value of a proposed satellite imager for ground
 1163 level particulate matter analyses and forecasts. *IEEE J. Sel. Top. Appl.*, **2**, 271–283, 2009b.
 1164
 1165 Timmermans, R.M.A., Lahoz, W.A., Attié, J.-L., Peuch, V.-H., Curier, R.L., Edwards, D.P.,
 1166 Eskes, H.J., Builtjes, P.J.H.: Observing System Simulation Experiments for air quality,
 1167 *Atmospheric Environment* doi: 10.1016/j.atmosenv.2015.05.032, 2015.
 1168
 1169 Tolk, L. F., Dolman, A. J., Meesters, A. G. C. A., and Peters, W.: A comparison of different
 1170 inverse carbon flux estimation approaches for application on a regional domain, *Atmos. Chem.*
 1171 *Phys.*, 11, 10349-10365, doi:10.5194/acp-11-10349-2011, 2011.
 1172
 1173 Weaver, A.T., Vialard, J., Anderson, D.L.T, Delecluse, P.: Three- and four-dimensional
 1174 variational assimilation with an ocean general circulation model of the tropical Pacific Ocean.
 1175 Part I: formulation, internal diagnostics and consistency checks, *Mon. Wea.Rev.*, 131, 1360-
 1176 1378, 2003.
 1177
 1178 World Meteorological Organization: “Scientific Requirements” in Report of the
 1179 WMO/UNEP/ICSU Meeting on Instruments, Standardization and measurement techniques for
 1180 atmospheric CO₂, Geneva, Switzerland, 8-11 September 1981.
 1181
 1182 Zhang, X., Gurney, K. R., Rayner, P., Baker, D., and Liu, Y.-P.: Sensitivity of simulated CO₂
 1183 concentration to sub-annual variations in fossil fuel CO₂ emissions, *Atmos. Chem. Phys.*
 1184 *Discuss.*, 15, 20679-20708, doi:10.5194/acpd-15-20679-2015, 2015.
 1185
 1186 Ziehn, T., Nickless, A., Rayner, P. J., Law, R. M., Roff, G., and Fraser, P.: Greenhouse gas
 1187 network design using backward Lagrangian particle dispersion modelling – Part 1: Methodology
 1188 and Australian test case, *Atmos. Chem. Phys.*, 14, 9363-9378, doi:10.5194/acp-14-9363-2014,
 1189 2014.

Table 1. Uncertainty reduction in two-week and European mean NEE for July and December as a function of the observation network and of the configuration of the inversion parameters (\mathbf{B}_{250} or \mathbf{B}_{150} for \mathbf{B} and \mathbf{R}_{ref} or \mathbf{R}_{red} for \mathbf{R}).

	Month	B	R	Prior uncertainty (TgCmonth ⁻¹)	Posterior uncertainty (TgCmonth ⁻¹)	NEE from ORCHIDEE (TgCmonth ⁻¹)	Uncertainty Reduction (%)
ICOS23	July	\mathbf{B}_{250}	\mathbf{R}_{ref}	91.2	42.6	-201.6	53
	December	\mathbf{B}_{250}	\mathbf{R}_{ref}	74.9	25.5	80.3	66
ICOS50	July	\mathbf{B}_{250}	\mathbf{R}_{ref}	91.2	32.4	-201.6	64
	December	\mathbf{B}_{250}	\mathbf{R}_{ref}	74.9	19.5	80.3	74
	July	\mathbf{B}_{250}	\mathbf{R}_{red}	91.2	30.4	-201.6	67
ICOS66	July	\mathbf{B}_{250}	\mathbf{R}_{ref}	91.2	32.8	-201.6	64
	December	\mathbf{B}_{250}	\mathbf{R}_{ref}	74.9	15.4	80.3	79
	July	\mathbf{B}_{150}	\mathbf{R}_{ref}	55.0	29.2	-201.6	47

1201 **Table A1.** Atmospheric measurement sites for the different ICOS network configurations
1202 considered in this study with associated observation errors in the reference configuration of the
1203 inversion. Two values are given for the observation error at a given site for low altitude sites:
1204 that for temporal window 12:00-18:00 (left) and temporal window 18:00-20:00 (right), and one
1205 value for temporal window 00:00-06:00 at high altitude sites. Height corresponds to the vertical
1206 location of the site above the ground level (magl) and elevation corresponds to its vertical
1207 location above sea level (masl).

1208

Network	Site	Country	Code	type	Lon	Lat	Height magl	Elevation masl	Assim. Window	Obs. Err. (ppm)	
										July	Dec
ICOS23	Bialystok	PL	bik	TT	23.01	53.23	300	480	12-20	4.2-7.2	10.2-15.2
	Biscarrose	FR	bis	G	-1.23	44.38	47	120	12-20	4.2-7.2	10.2-15.2
	Cabauw	NL	cbw	TT	4.93	51.97	200	200	12-20	4.2-7.2	10.2-15.2
	Monte Cimone	IT	cmn	G	10.68	44.17	12	2177	00-06	3.6	3.6
	Gif-sur-Yvette	FR	gif	G	2.15	48.71	7	167	12-20	4.2-7.2	10.2-15.2
	Heidelberg	DE	hei	G	8.67	49.42	30	146	12-20	4.2-7.2	10.2-15.2
	Hegyhatsal	HN	hun	TT	16.65	46.96	115	363	12-20	4.2-7.2	10.2-15.2
	Jungfraujoch	CH	jfj	G	7.98	46.55	gl	3580	00-06	3.6	3.6
	Kasprowy Wierch	PL	kas	G	19.98	49.23	gl	1987	00-06	3.6	3.6
	Lampedusa	IT	lmp	G	12.63	35.52	8	58	12-20	4.2-7.2	10.2-15.2
	La Muela	ES	lmu	TT	-1.1	41.59	79	649	12-20	4.2-7.2	10.2-15.2
	Lutjewad	NL	lut	G	6.35	53.4	60	61	12-20	4.2-7.2	10.2-15.2
	Mace Head	IR	mhd	G	-9.9	53.33	15	40	12-20	4.2-7.2	10.2-15.2
	Ochsenkopf	DE	oxk	TT	11.81	50.03	163	1185	00-06	3.6	3.6
	Pallas	FI	pal	G	24.12	67.97	5	565	12-20	4.2-7.2	10.2-15.2
	Plateau Rosa	IT	prs	G	7.7	45.93	gl	3480	00-06	3.6	3.6
	Puy de Dôme	FR	puy	G	2.97	45.77	10	1475	00-06	3.6	3.6
	Schauinsland	DE	sch	G	7.92	47.9	gl	1205	00-06	3.6	3.6
	Trainou	FR	trn	TT	2.11	47.96	180	311	12-20	4.2-7.2	10.2-15.2
	Westerland	DE	wes	G	8.32	54.93	gl	12	12-20	4.2-7.2	10.2-15.2
	Angus	UK	tta	TT	-2.98	56.56	220	520	12-20	4.2-7.2	10.2-15.2
	Egham	UK	egh	G	-0.55	51.43	5	45	12-20	4.2-7.2	10.2-15.2
	Norunda	SE	nor	TT	17.48	60.09	102	147	12-20	4.2-7.2	10.2-15.2
ICOS50	Kresin u Pacova	CZ	kre	TT	15.08	49.57	250	790	12-20	4.2-7.2	10.2-15.2
	Hohenpeißenberg	DE	hpb	TT	11.01	47.8	159	1106	00-06	3.6	3.6
	Zugspitze	DE	zug	G	10.98	47.42	10	2660	00-06	3.6	3.6
	Risø Meteorological Mast	DK	ris	TT	12.09	55.65	125	130	12-20	4.2-7.2	10.2-15.2
	Høvsøre Wind Test Station	DK	hov	TT	8.15	56.44	116	116	12-20	4.2-7.2	10.2-15.2
	Carnsore Point EMEP monitoring Station	IR	crn	G	-6.33	52.06	3	3	12-20	4.2-7.2	10.2-15.2
	Malin Head Synoptic Meteorological Station	IR	mld	G	-7.37	55.38	3	13	12-20	4.2-7.2	10.2-15.2
	Katowice Kosztowy	PL	kat	TT	19.12	50.19	355	655	12-20	4.2-7.2	10.2-15.2

	Piła Rusionow	PL	pil	TT	16.26	53.17	320	455	12-20	4.2-7.2	10.2-15.2
	Jemiolow	PL	jem	TT	15.28	52.35	314	475	12-20	4.2-7.2	10.2-15.2
	Hyltemossa	SE	hyl	TT	13.42	56.1	150	255	12-20	4.2-7.2	10.2-15.2
	Observatoire Pérenne de l'Environnement	FR	ope	TT	5.36	48.48	120	512	12-20	4.2-7.2	10.2-15.2
	Observatoire de Haute Provence	FR	ohp	TT	5.71	43.93	100	740	12-20	4.2-7.2	10.2-15.2
	Pic du Midi	FR	pdm	G	0.14	42.94	10	2887	00-06	3.6	3.6
	SMEAR II Hyytiälä	FI	hyy	TT	24.29	61.85	127	308	12-20	4.2-7.2	10.2-15.2
	Puijo-Koli	FI	pui	TT	27.65	62.9	176	406	12-20	4.2-7.2	10.2-15.2
	ICOS eastern Finland Utö - Baltic sea	FI	uto	G	21.38	59.78	60	68	12-20	4.2-7.2	10.2-15.2
	Finokalia	GR	fik	G	25.67	35.34	2	152	12-20	4.2-7.2	10.2-15.2
	Birkenes Observatory	NO	bir	G	8.25	58.38	gl	190	12-20	4.2-7.2	10.2-15.2
	Andøya Observatory	NO	and	G	16.01	69.27	gl	380	12-20	4.2-7.2	10.2-15.2
	Svartberget	SE	sva	TT	19.78	64.26	150	385	12-20	4.2-7.2	10.2-15.2
	Tacolneston (norfolk)	UK	tac	G	1.14	52.52	191	261	12-20	4.2-7.2	10.2-15.2
	Ridge Hill	UK	rhi	G	-2.54	52	152	356	12-20	4.2-7.2	10.2-15.2
	Delta Ebre	ES	dec	TT	0.79	40.74	11	16	12-20	4.2-7.2	10.2-15.2
	Valderejo	ES	val	TT	-3.21	42.87	25	1100	00-06	3.6	3.6
	Xures-Invernadeiro	ES	xic	TT	-8.02	41.98	30	902	12-20	4.2-7.2	10.2-15.2
	Ispra	IT	isp	G	8.63	45.81	40	230	12-20	4.2-7.2	10.2-15.2
ICOS66	Lindenberg	DE	lin	TT	14.12	52.21	99	192	12-20	4.2-7.2	10.2-15.2
	Mannheim	DE	man	TT	8.49	49.49	213	323	12-20	4.2-7.2	10.2-15.2
	Gartow 2	DE	grt	TT	11.44	53.07	344	410	12-20	4.2-7.2	10.2-15.2
	Messkirch/Rohrdorf	DE	msr	TT	9.12	48.02	240	892	12-20	4.2-7.2	10.2-15.2
	Wesel	DE	wsl	TT	6.57	51.65	321	340	12-20	4.2-7.2	10.2-15.2
	Helgoland	DE	hlg	G	7.9	54.18	10	40	12-20	4.2-7.2	10.2-15.2
	Iznajar	ES	izn	TT	-4.38	37.28	5	555	12-20	4.2-7.2	10.2-15.2
	Hengelo	NL	hen	G	6.75	52.34	70	80	12-20	4.2-7.2	10.2-15.2
	Goes	NL	goe	G	3.78	51.48	70	70	12-20	4.2-7.2	10.2-15.2
	Peel	NL	pee	G	5.98	51.37	70	80	12-20	4.2-7.2	10.2-15.2
	Noordzee	NL	nse	G	4.73	54.85	50	50	12-20	4.2-7.2	10.2-15.2
	Cap Corse	FR	cor	G	9.35	42.93	35	85	12-20	4.2-7.2	10.2-15.2
	Roc Tredudon	FR	roc	G	-3.91	48.41	10	373	12-20	4.2-7.2	10.2-15.2
	Alfabia	ES	alf	TT	2.72	39.74	gl	1069	00-06	3.6	3.6
	Saissac	FR	sai	TT	2.1	43.39	300	800	00-06	3.6	3.6
	NIO	FR	nio	TT	0.05	46.19	330	503	12-20	4.2-7.2	10.2-15.2

1209

1210

1211

1212 **Table A2.** NEE uncertainty budget for European countries for July 2007 estimated using the
1213 reference inversion configuration and different atmospheric CO₂ networks. Uncertainty
1214 reduction values (UR) are shown in the last two columns for ICOS23 and ICOS66.

Country	NEE, TgCcountry ⁻¹ month ⁻¹	NEE prior unc. TgCcountry ⁻¹ month ⁻¹	NEE post. Unc.		UR (%)	
			TgCcountry ⁻¹ month ⁻¹			
			ICOS23	ICOS66	ICOS23	ICOS66
Austria	-3.95	4.60	1.49	1.56	68	66
Belgium	-1.05	1.88	0.69	0.69	63	63
Bulgaria	-1.22	5.72	5.43	4.06	5	29
Croatia	-1.64	2.27	1.17	1.13	48	50
Cyprus	0.04	0.18	0.18	0.18	0	1
Czech Republic	-4.35	4.08	2.06	1.52	50	63
Denmark	-1.97	1.74	1.35	0.76	22	57
Estonia	-2.67	2.37	1.66	1.42	30	40
Finland	-8.37	11.56	5.92	3.14	49	73
France	-17.16	18.41	3.52	3.04	81	84
Germany	-16.00	14.20	4.73	2.73	67	81
Greece	0.09	3.58	3.45	2.89	4	19
Hungary	-2.19	4.95	2.61	2.31	47	53
Ireland	-2.49	2.42	1.68	1.27	30	48
Italy	-4.44	9.83	4.24	3.82	57	61
Latvia	-3.61	3.32	2.33	2.22	30	33
Lithuania	-3.92	3.42	2.02	2.10	41	39
Luxembourg	-0.12	0.17	0.10	0.10	42	44
Netherlands	-0.97	1.99	0.65	0.50	68	75
Norway	-6.02	9.65	4.85	4.65	50	52
Poland	-21.10	13.26	5.02	4.24	62	68

Portugal	-1.17	4.24	3.71	2.80	12	34
Romania	-7.14	10.79	9.14	8.34	15	23
Slovakia	-2.82	2.59	1.30	1.30	50	50
Slovenia	-1.17	1.04	0.48	0.43	54	58
Spain	-3.54	19.90	7.16	3.97	64	80
Sweden	-9.84	16.50	7.53	5.62	54	66
Switzerland	-1.72	2.61	1.03	0.68	60	74
UK	-8.52	7.56	2.11	1.59	72	79

1215

1216

1217

1218

1219

1220

1221

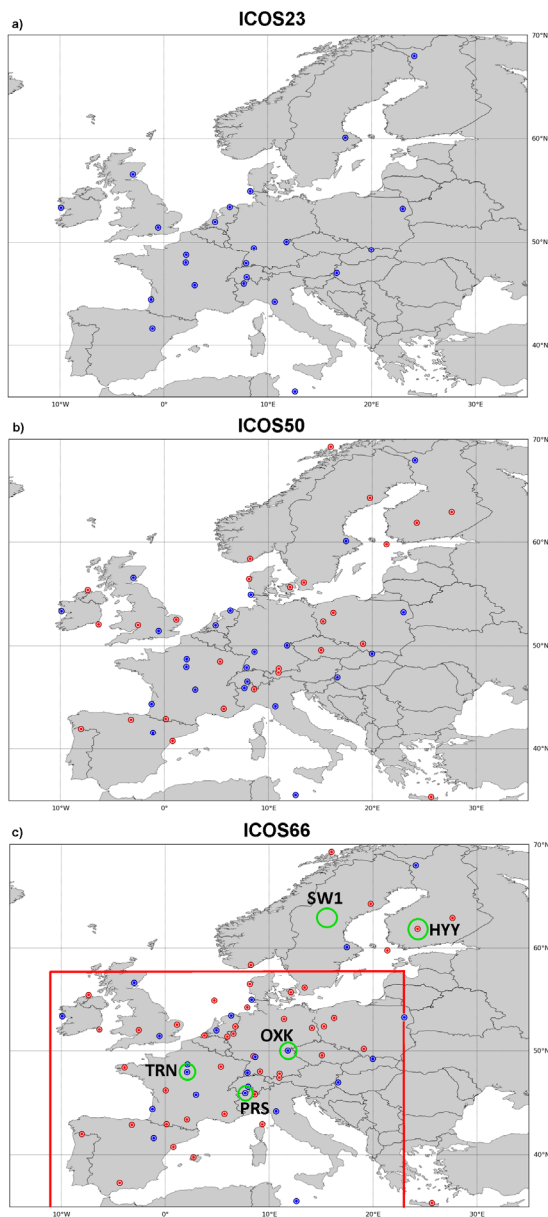


Figure 1. Site location for the different ICOS network configurations used in this study: (a)

ICOS23 (b) ICOS50 (c) ICOS66. Dark blue circles correspond to ICOS23 and the red circles are the new sites for ICOS50 and ICOS66 compared to ICOS23. The European domain ($\sim 6.8 \times 10^6$ km² of land surface) covered by these figures corresponds to the domain of the configuration of the CHIMERE atmospheric transport model used in this study. The red rectangle in (c)

1228 corresponds to a western European domain (WE domain, $\sim 3.5 * 10^6$ km² of land surface) which
1229 is used for some of the present analysis because it is significantly better sampled by the ICOS
1230 networks than other areas. Green circles in (c) are the station locations used for the study of the
1231 uncertainty reduction as a function of the spatial scale of the aggregation around each station (in
1232 Sect. 3.1.4).

1233

1234

1235

1236

1237

1238

1239

1240

1241

1242

1243

1244

1245

1246

1247

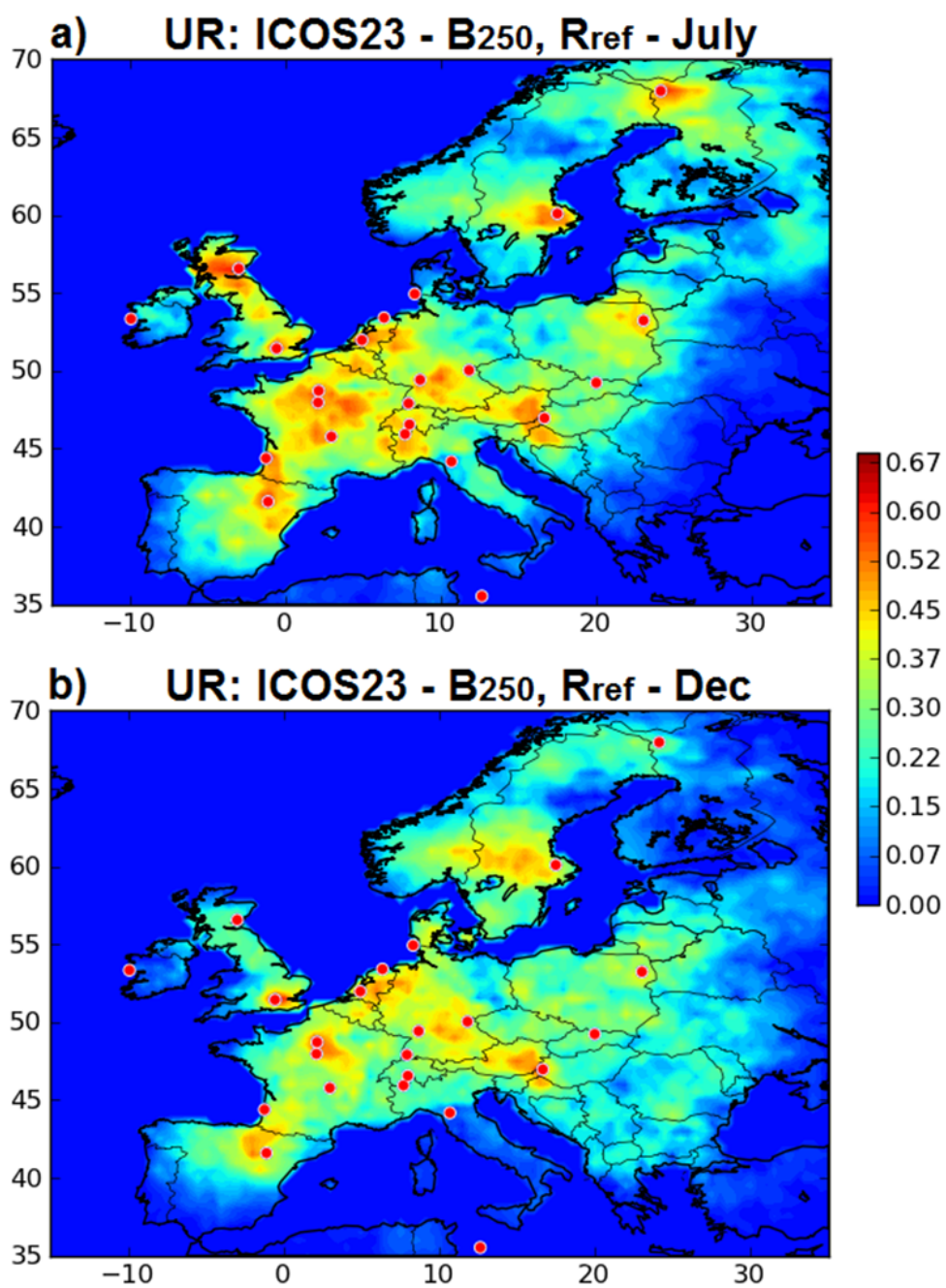


Figure 2. Uncertainty reduction (theoretically comprised between 0 and 1) for two-week mean NEE at 0.5° resolution in July (a) and in December (b) when using ICOS23 (red dots) and the

1251 reference inversion set-up. Red/blue colors indicate relatively high/low uncertainty reduction
1252 (with min = 0, max = 0.68 in the color scale).

1253

1254

1255

1256

1257

1258

1259

1260

1261

1262

1263

1264

1265

1266

1267

1268

1269

1270

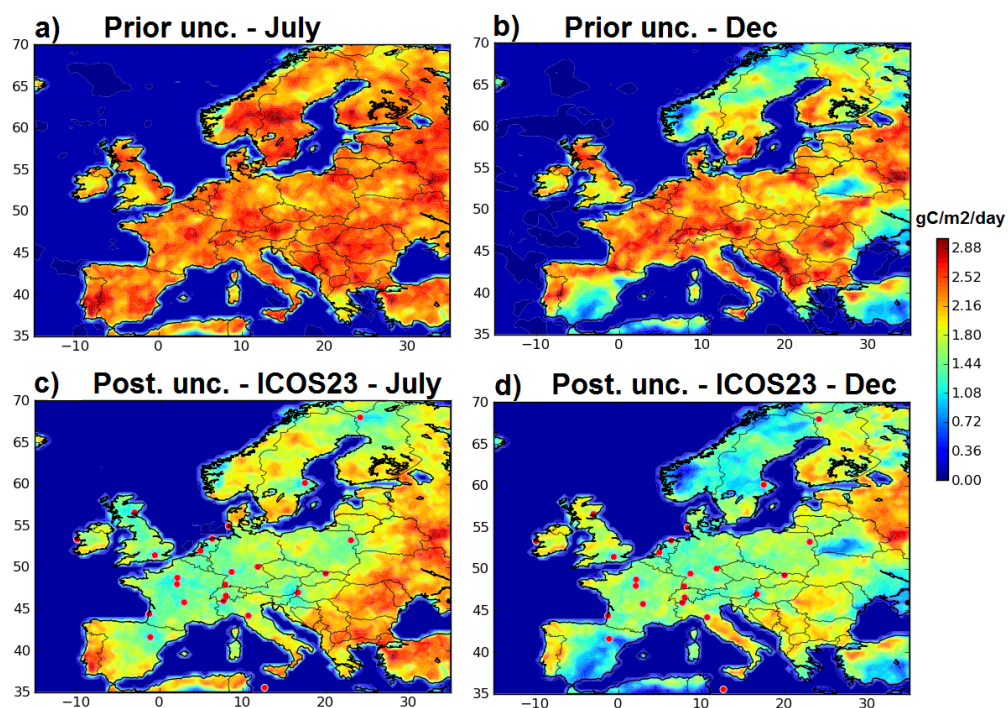


Figure 3. Standard deviations ($\text{gCm}^{-2}\text{day}^{-1}$) of the prior (a,b) and posterior (c,d) uncertainties in two-week mean NEE at 0.5° resolution for (a,c) July and (b,d) December. Posterior uncertainties are given for inversions using ICOS23 (red dots) and the reference inversion set-up. Red/blue colors indicate relatively high/low uncertainties (with $\text{min} = 0 \text{ gCm}^{-2}\text{day}^{-1}$, $\text{max} = 3 \text{ gCm}^{-2}\text{day}^{-1}$ in the color scale).

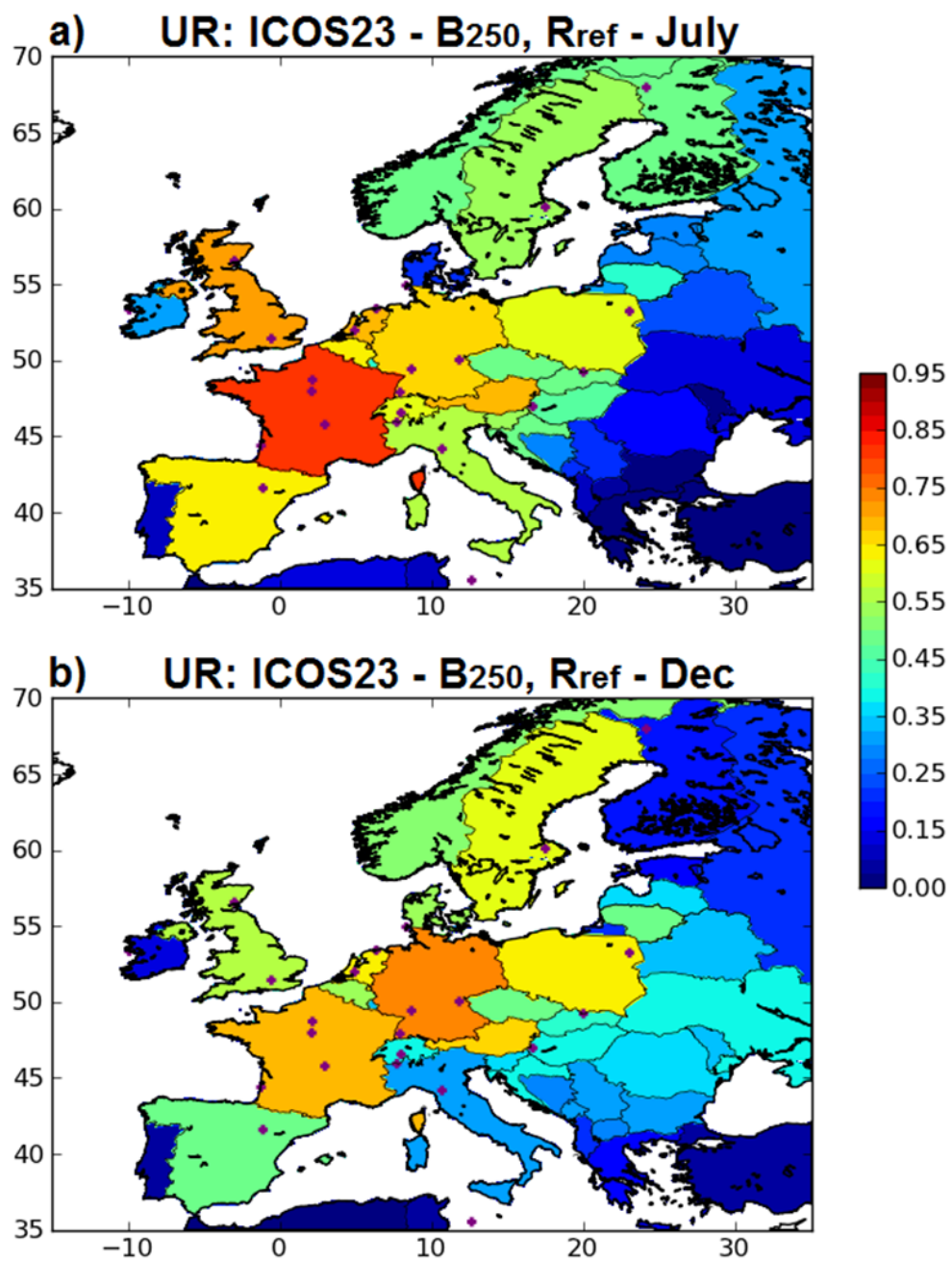


Figure 4. Uncertainty reduction (theoretically comprised between 0 and 1) for two-week mean NEE at the country scale for July (a) and December (b) when using ICOS23 and the reference

1286 inversion configuration. Red/blue colors indicate relatively high/low uncertainty reduction (with
1287 min = 0, max = 0.95 in the color scale).

1288

1289

1290

1291

1292

1293

1294

1295

1296

1297

1298

1299

1300

1301

1302

1303

1304

1305

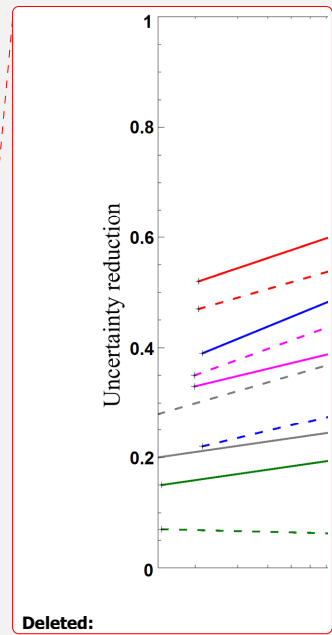
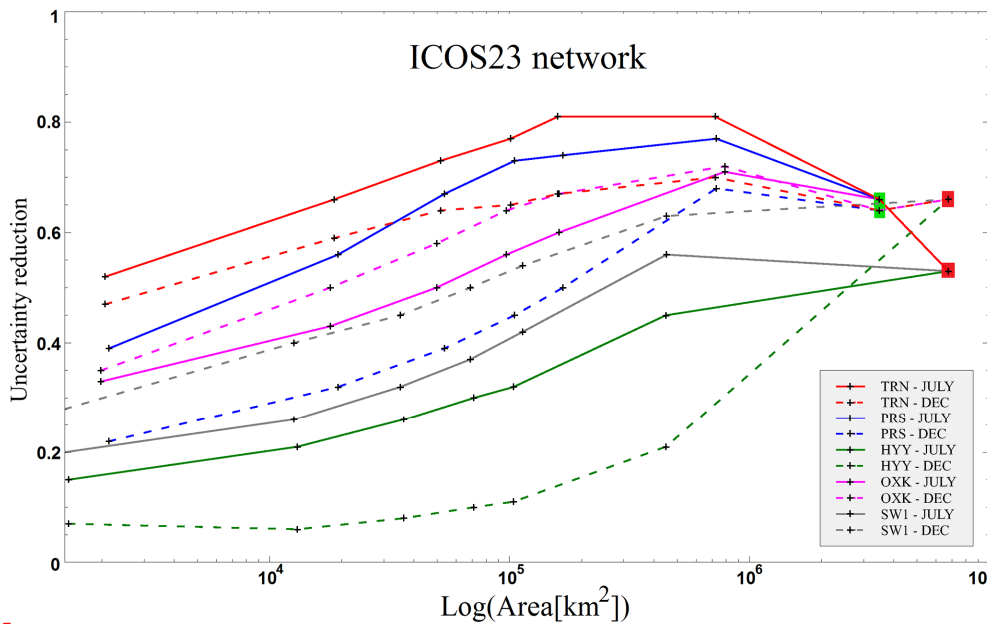


Figure 5. Uncertainty reduction (theoretically comprised between 0 and 1) for two-week mean NEE in July and December 2007 using ICOS23 and the reference configuration of the inversion, as a function of the size (logarithmic scale) of the spatial averaging area (in km², as indicated by the crosses, for each curve values are derived for 1.5°x1.5°, 2.5°x2.5°, 3.5°x3.5°, 4.5°x4.5° and 10.5°x10.5° areas which correspond to different values in terms of km² depending on their location in Europe) around each station TRN (red curves), PRS (blue curves), HYY (green curves), OXK (pink curves) and SW1 (grey curves; see the locations in Fig. 1c). Solid and dash lines correspond to results for July and December respectively (see the legend within the figure). The results of uncertainty reduction for the whole European domain are included (red rectangles). The results for the western European domain defined in Fig. 1c are included on curves corresponding to sites which are located in this domain (TRN, PRS and OXK, see the green rectangles).

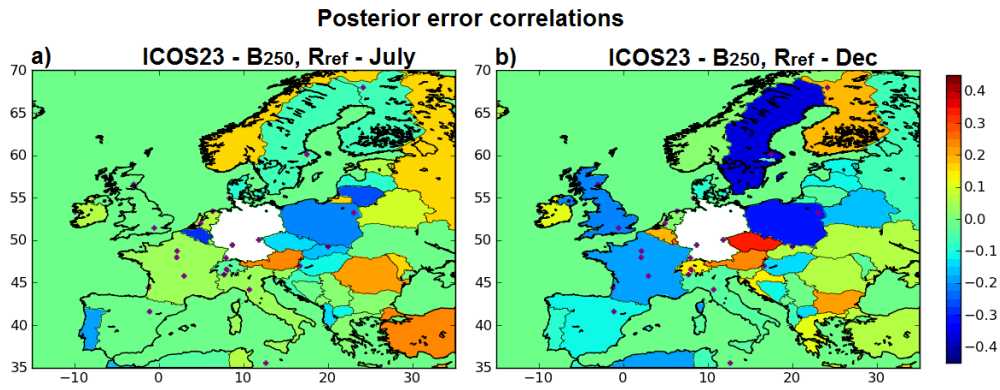
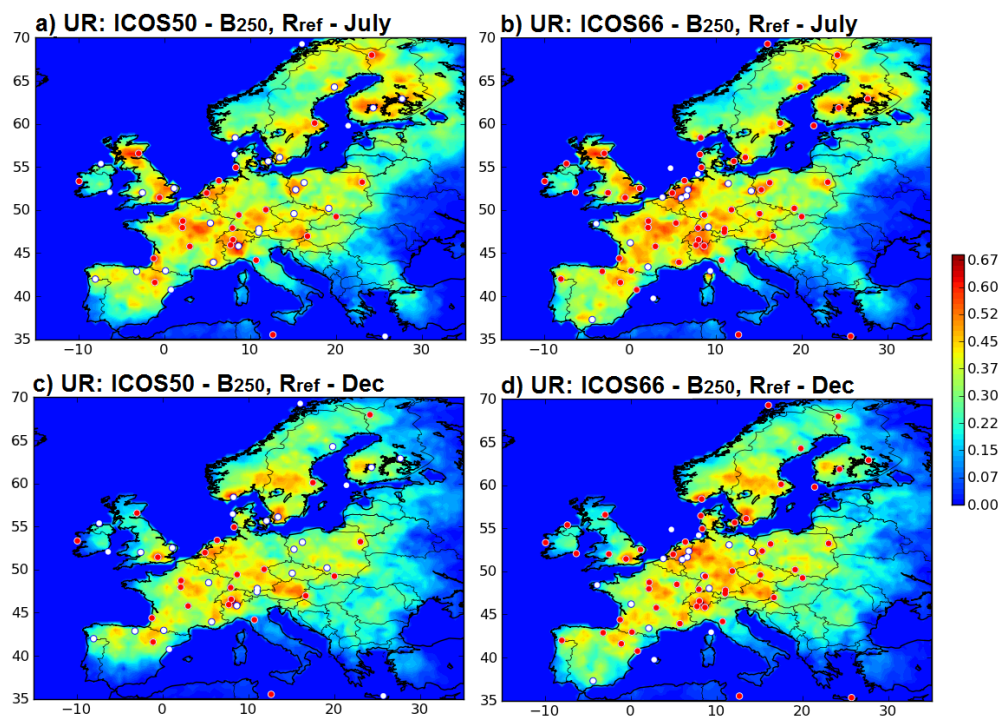


Figure 6. Correlations of the posterior uncertainties in two-week mean NEE between Germany and the other European countries in July (a) and December (b) from the reference inversions with ICOS23. Germany is masked in white. Red/blue colors indicate relatively high positive/negative correlations (with min= -0.45, max = 0.45 in the color scale).

1338



1339

1340 **Figure 7.** Uncertainty reduction (theoretically comprised between 0 and 1) for two-week mean
 1341 NEE at 0.5° resolution in July (a,b) and December (c,d) when using ICOS50 (a,c) and ICOS66
 1342 (b,d) and the reference inversion configuration. Red dots corresponds to the ICOS23 (a,c) or
 1343 ICOS50 (b,d) sites while white dots correspond to the additional sites included in ICOS50 or
 1344 ICOS66 respectively. Red/blue colors indicate relatively high/low uncertainty reduction (with
 1345 min = 0, max = 0.68 in the color scale).

1346

1347

1348

1349

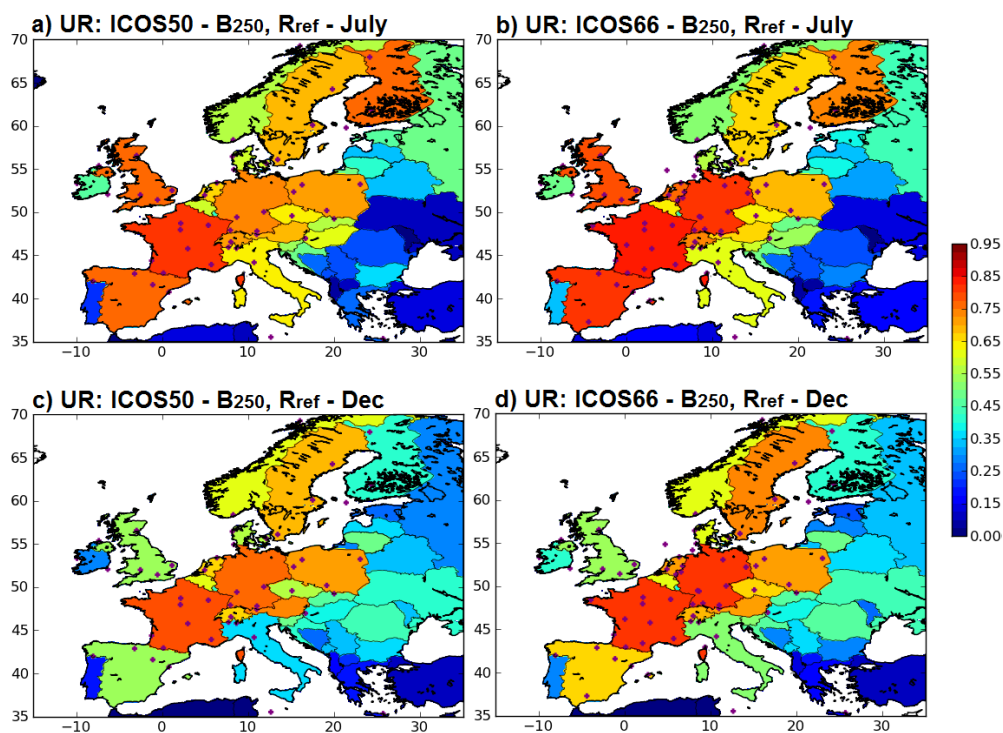


Figure 8. Uncertainty reduction (theoretically comprised between 0 and 1) for two-week mean NEE at the country scale in July (a,b) and December (c,d), when using ICOS50 (a,c) and ICOS66 (b,d). Red/blue colors indicate relatively high/low uncertainty reduction (with min = 0, max = 0.95 in the color scale).

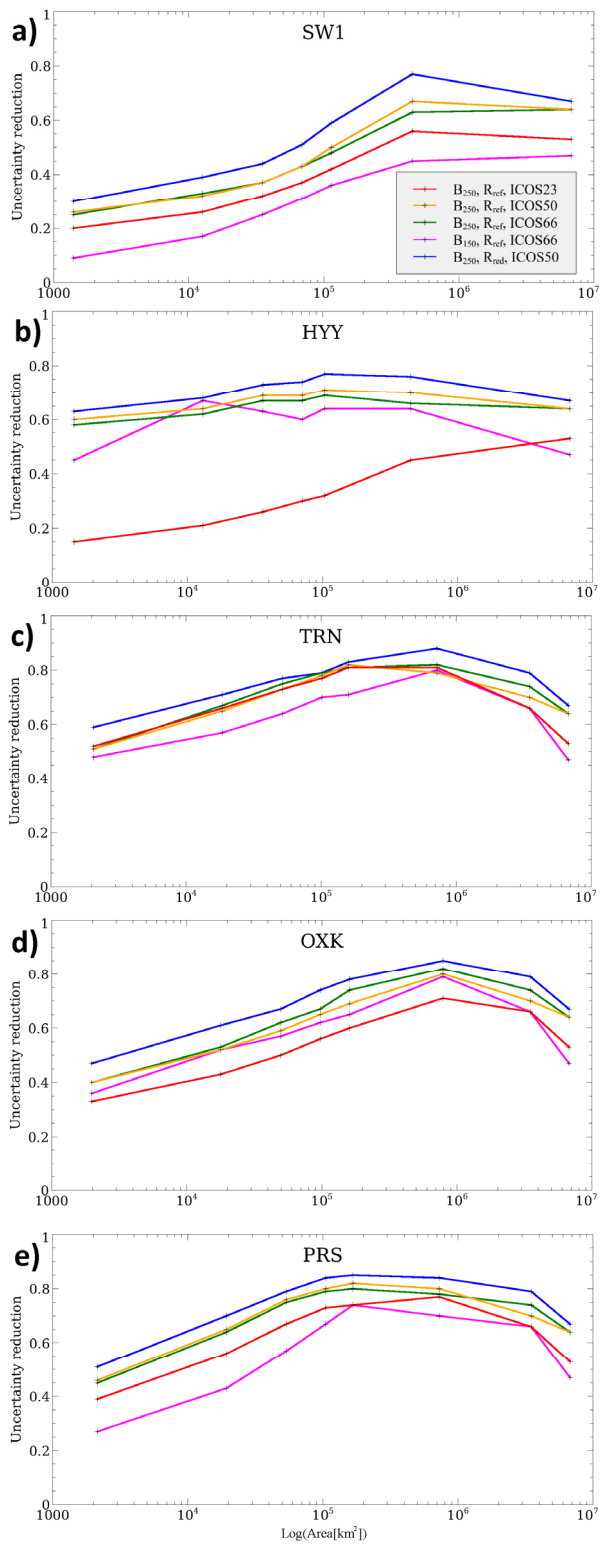


Figure 9. Uncertainty reduction (theoretically comprised between 0 and 1) for two-week mean NEE for July 2007 as a function of the size (in logarithmic scale) of the spatial averaging area (same as for Fig. 5) centered on **(a)** SW1, **(b)** HYY, **(c)** TRN, **(d)** OXK, and **(e)** PRS. Red, orange, green lines: results with the reference configuration of the inversion using ICOS23, ICOS50 and ICOS66 respectively; blue: results when using ICOS50 and the inversion configuration with $\mathbf{R}=\mathbf{R}_{\text{red}}$; pink: results when using ICOS66 and the inversion configuration with $\mathbf{B}=\mathbf{B}_{150}$. The results of uncertainty reduction for the whole European domain are included systematically. The results for the western European domain defined in Fig. 1c are included on curves corresponding to sites which are located in this domain (TRN, PRS and OXK).

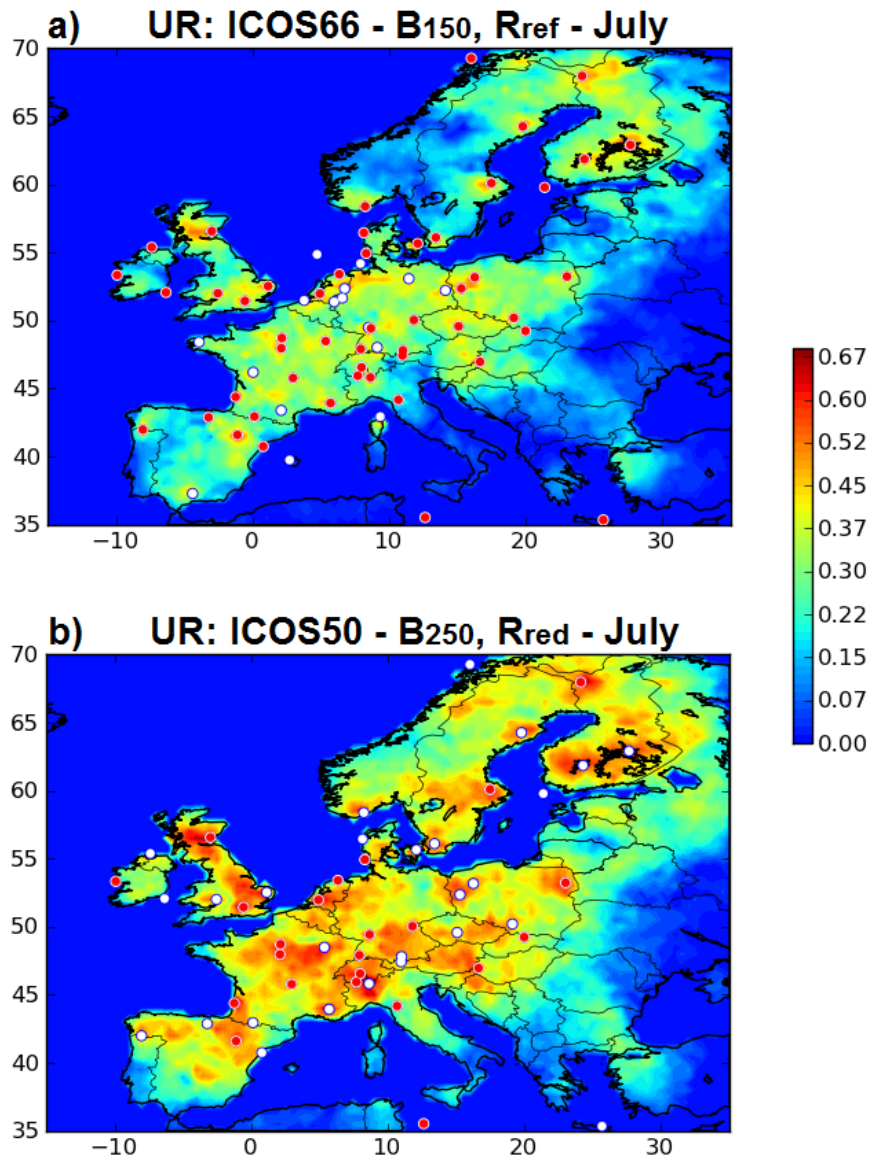


Figure 10. Uncertainty reduction (theoretically comprised between 0 and 1) for two-week mean NEE at 0.5° horizontal resolution in July when modifying the inversion configuration from the reference one: using B_{150} instead of B_{250} and ICOS66 (a) using R_{red} instead of R_{ref} and ICOS50 (b). Red dots corresponds to the ICOS23 (b) or ICOS50 (a) sites while white dots correspond to the additional sites included in ICOS50 or ICOS66 respectively. Red/blue colors indicate relatively high/low uncertainty reduction (with min = 0, max = 0.68 in the color scale).

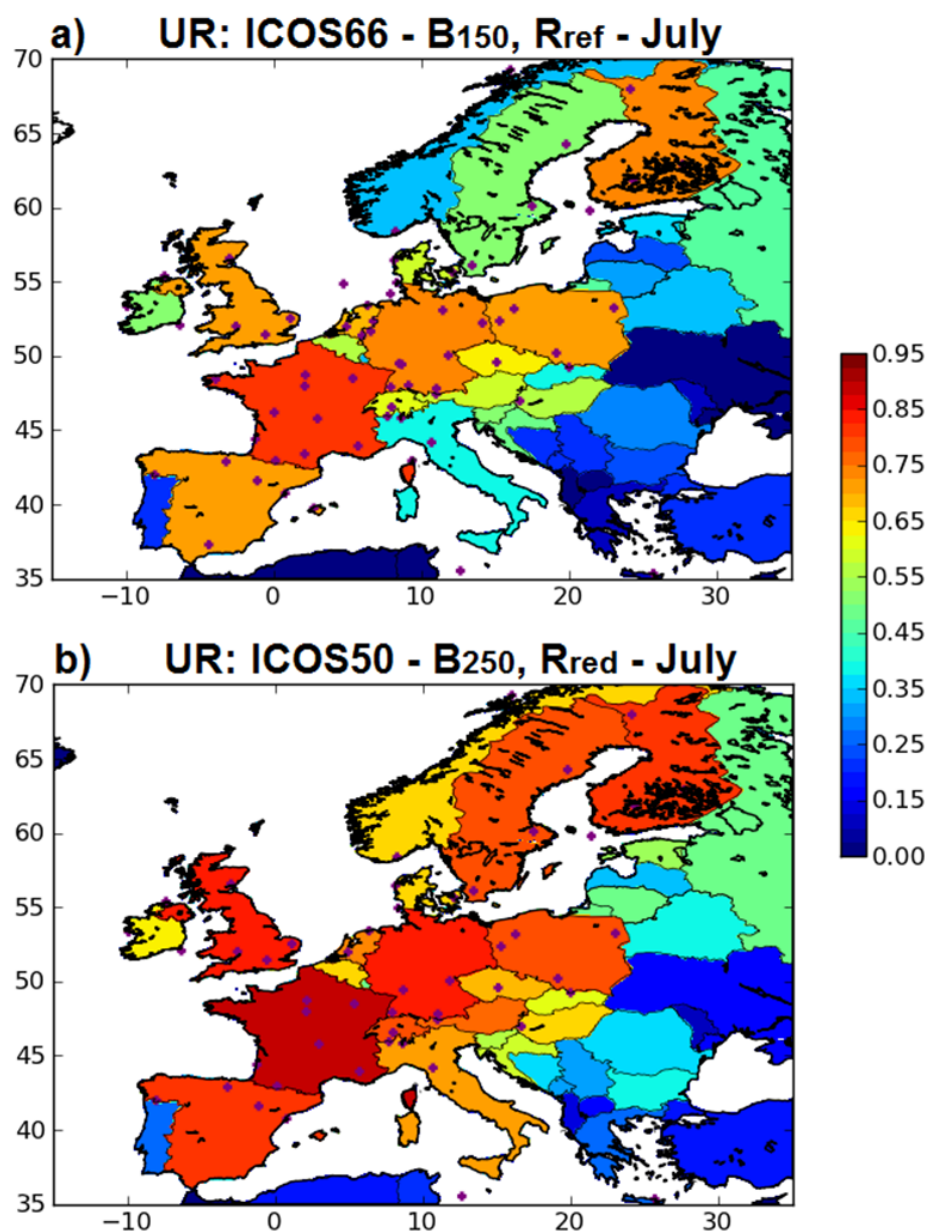


Figure 11. Uncertainty reduction (theoretically comprised between 0 and 1) for two-week mean NEE at the country scale in July when modifying the inversion configuration from the reference one by using B_{150} instead of B_{250} and ICOS66 (a) using R_{red} instead of R_{ref} and ICOS50 (b).

1393 Red/blue colors indicate relatively high/low uncertainty reduction (with min = 0, max = 0.95 in
1394 the color scale).

1395

1396

1397

1398

1399

1400

1401

1402

1403

1404

1405

1406

1407

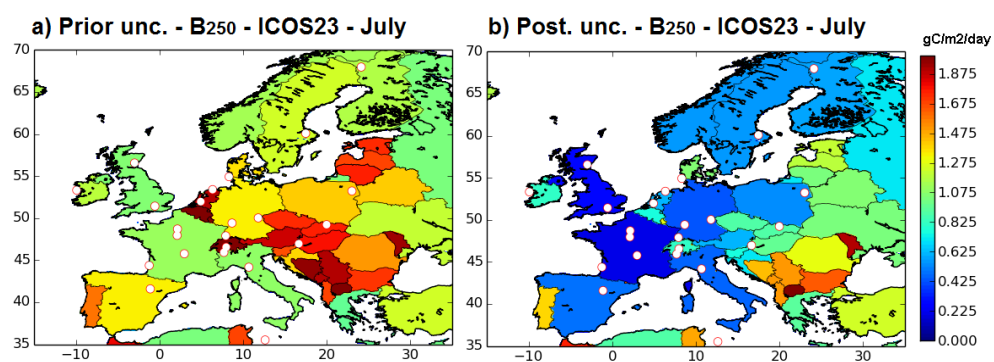


Figure 12. Standard deviations ($\text{gCm}^{-2}\text{day}^{-1}$) of the prior (a) and posterior (b) flux uncertainties at country scale. Posterior uncertainties are given for inversions using ICOS23 (white circles) and the reference inversion set-up. Red/blue colors indicate relatively high/low uncertainties (with $\text{min} = 0 \text{ gCm}^{-2}\text{day}^{-1}$, $\text{max} = 1.975 \text{ gCm}^{-2}\text{day}^{-1}$ in the color scale).

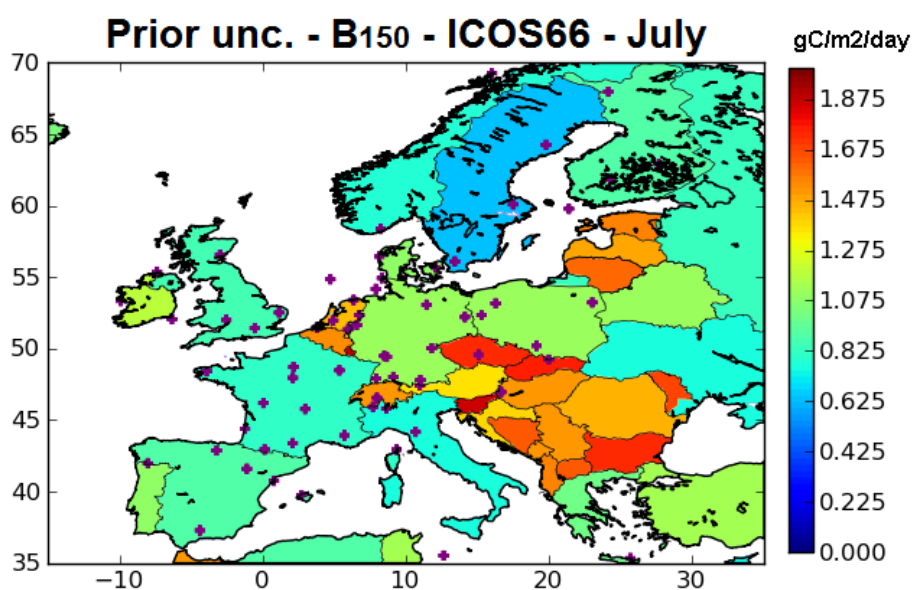


Figure A1. Standard deviations ($\text{gCm}^{-2}\text{day}^{-1}$) of the prior flux uncertainties at country scale for July when considering \mathbf{B}_{150} . Red dots: ICOS66. Red/blue colors indicate relatively high/low uncertainties (with min = 0 $\text{gCm}^{-2}\text{day}^{-1}$, max = 1.975 $\text{gCm}^{-2}\text{day}^{-1}$ in the color scale).

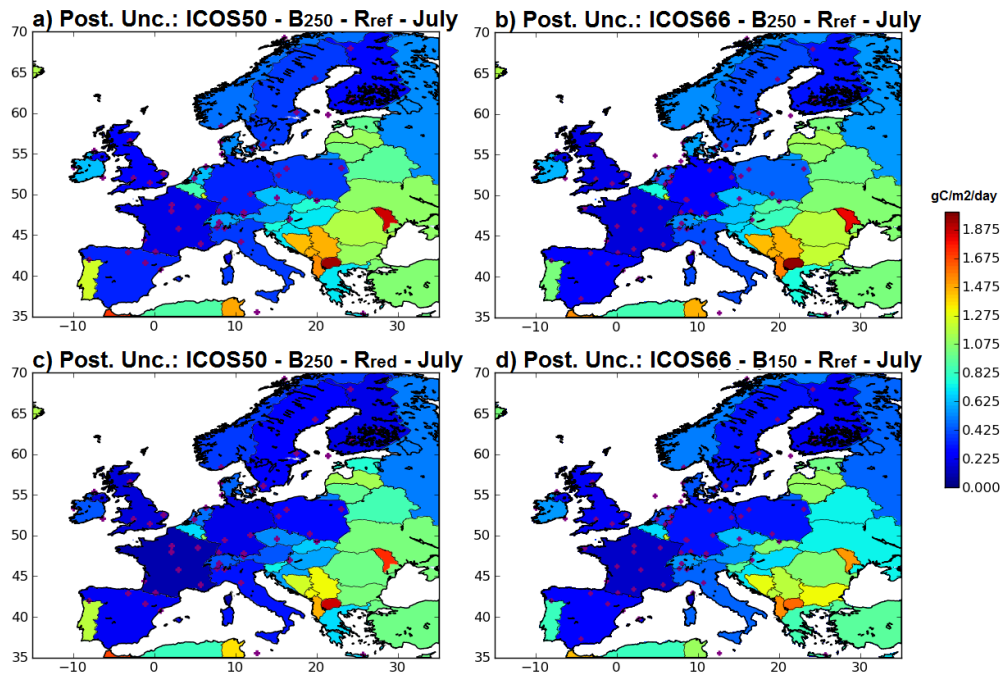


Figure A2. Standard deviations ($\text{gCm}^{-2}\text{day}^{-1}$) of the posterior uncertainties at country scale for July when using ICOS50 (a,c) and ICOS66 (b,d), the reference inversion configuration (a,b), using \mathbf{B}_{150} instead of \mathbf{B}_{250} (d) using \mathbf{R}_{red} instead of \mathbf{R}_{ref} (c). Red/blue colors indicate relatively high/low uncertainties (with $\text{min} = 0 \text{ gCm}^{-2}\text{day}^{-1}$, $\text{max} = 1.975 \text{ gCm}^{-2}\text{day}^{-1}$ in the color scale).

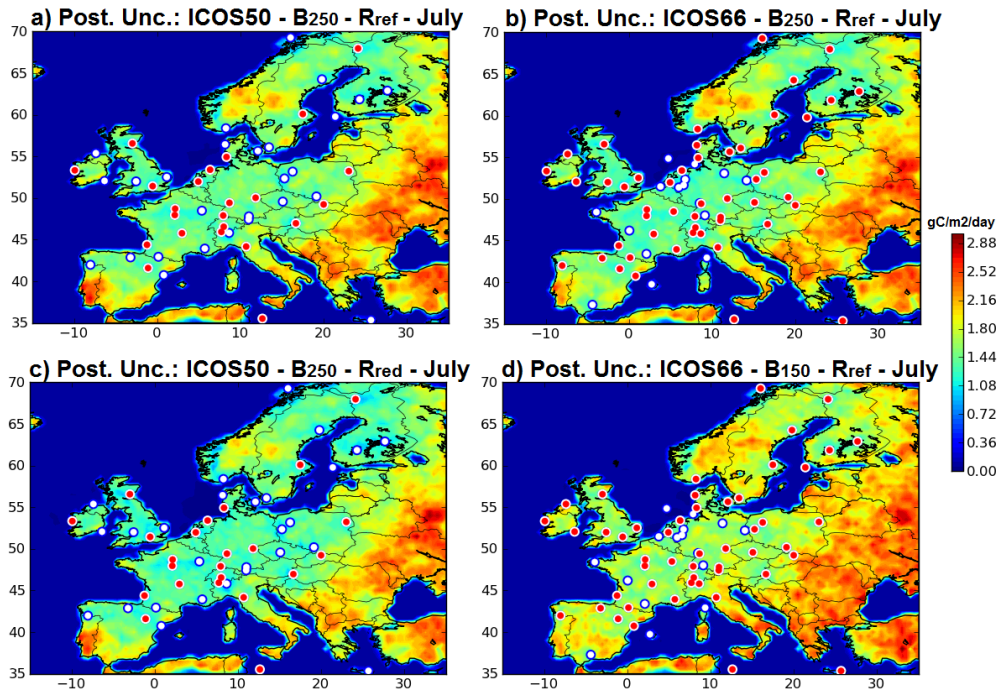


Figure A3. Standard deviations ($\text{gCm}^{-2}\text{day}^{-1}$) of the posterior uncertainties in two-week mean NEE at 0.5° resolution for July when using ICOS50 (a,c) and ICOS66 (b,d), the reference inversion configuration (a,b), using \mathbf{B}_{150} instead of \mathbf{B}_{250} (d) using \mathbf{R}_{red} instead of \mathbf{R}_{ref} (c). Red dots corresponds to the ICOS23 (a,c) or ICOS50 (b,d) sites while white dots correspond to the additional sites included in ICOS50 or ICOS66 respectively. Red/blue colors indicate relatively high/low uncertainties (with $\text{min} = 0 \text{ gCm}^{-2}\text{day}^{-1}$, $\text{max} = 3 \text{ gCm}^{-2}\text{day}^{-1}$ in the color scale).